Metallurgical reactions and tribological properties of self-lubricating Al-WS$_2$ composites: Laser powder bed fusion Vs. spark plasma sintering

Peifeng Li [a], Fang Xu [a,*], Stuart Robertson [b], Zhaoxia Zhou [b], Xianghui Hou [a], Adam T. Clare [c,d], Nesma T. Aboulkhair [e,f]

[a] Faculty of Engineering, University of Nottingham, University Park, Nottingham NG7 2RD, UK
[b] Loughborough Materials Characterisation Centre, Department of Materials, Loughborough University, Loughborough LE11 3TU, UK
[c] Advanced Component Engineering Laboratory (ACEL), University of Nottingham, Nottingham NG7 2RD, UK
[d] Department of Mechanical, Materials and Manufacturing Engineering, Faculty of Science and Engineering, University of Nottingham China, 199 Taikang East Road, University Park, Ningbo 315100, China
[e] Centre for Additive Manufacturing, Advanced Manufacturing Building, University of Nottingham, NG8 1BB, UK
[f] Additive Manufacturing Laboratory, Advanced Materials Research Centre (AMRC), Technology Innovation Institute (TII), Masdar City, P.O. 9639, Abu Dhabi, United Arab Emirates

HIGHLIGHTS

- Al-WS$_2$ composites were fabricated by laser-based additive manufacturing and compared to spark plasma sintered counterparts.
- Products of reactions between Al and WS$_2$ were revealed by electron microscopy and yielded increased hardness.
- Worn surface evolution analysis was deployed to visualize the tribo-layer development from breakdown to re-formation.
- Laser powder bed fusion parts showed lower wear-affected depth compared to spark plasma sintered counterparts.

GRAPHICAL ABSTRACT
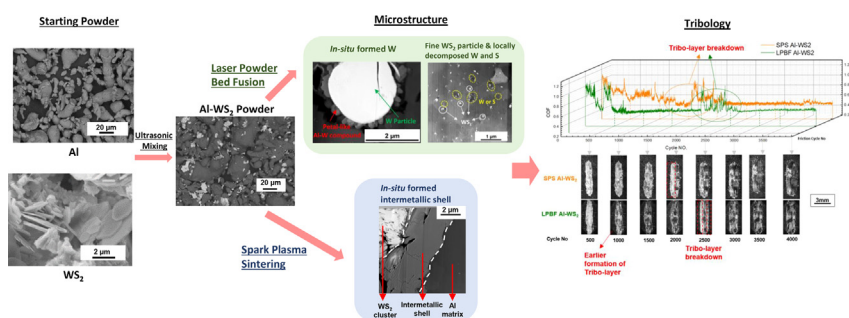
ARTICLE INFO

ABSTRACT

Self-lubricating aluminium-based composites reinforced with solid lubricants promise to meet the demand for lightweight materials in green tribological applications. The design advantages granted by additive manufacturing (AM) processes coupled with their capacity for in-situ production of composite materials are yet to be exploited in the realm of Al-transition metal dichalcogenides composites. In this work, laser powder bed fusion (LPBF) was deployed for the in-situ fabrication of Al-WS$_2$ composites for the first time, elucidating the process-structure–property relationships in comparison to reference spark plasma sintering (SPS) samples. The WS$_2$ response to the respective fabrication technique was also firstly investigated through a holistic characterisation. The formation of new phases (W for LPBF, Al$_5$W and Al$_{12}$W for SPS) provided the potential for microstructural tailoring for optimal tribological performance. For tribological properties, LPBF Al-WS$_2$ exhibited a coefficient of friction (COF) 0.55 ± 0.01 and specific wear rate 3.4 ± 0.3 × 10^{-3} mm^3/N·m, slightly better than the SPS counterpart (COF 0.57 ± 0.02, specific wear rate 3.6 ± 0.3 × 10^{-3} mm^3/N·m). Furthermore, a novel methodology for studying the evolution of worn surfaces is proposed and validated, by which a tribo-layer formed at lower friction cycles was observed for the LPBF samples, meaning that AM will also be advantageous for the performance aspect of self-lubricating materials.

---

* Corresponding author at: Room C46 Coates Building, University Park, Nottingham NG7 2RD, UK.
E-mail address: fang.xu@nottingham.ac.uk (F. Xu).

1. Introduction

Aluminium alloys have great potential in various sectors, including automotive and aerospace, thanks to their lightweight and excellent specific strength [1]. However, the tribological performance of Al is not as attractive, due to its soft nature. Traditionally, the tribological properties of Al are enhanced by improving their mechanical strength by alloying [2] and/or metal hardening techniques, such as work hardening and severe plastic deformation (SPD) [3,4]. Protective coatings can be used for counterbalance, but issues like degradation, difficulties in replenishment, and lack of compatibility with the substrate material arise [5]. Al metal matrix composites (MMCs) offer enhanced wear properties. These Al MMCs can be either wear-resistant (using hard brittle ceramic particles, such as Al_2O_3 [6] and SiC [7]) or self-lubricating (solid lubricants with laminated crystallographic structure), depending on the reinforcement [1]. The atoms in the lamellar crystal structure of solid lubricants are strongly bonded via covalent bonds within the sheet and weakly connected by Van der Waals force between layers. Therefore, the solid lubricant can be sheared easily parallel to the layers but is hard to break within the layer, which results in the reduction of friction by the relative motion between layers. Graphite is the most commonly studied self-lubricating additive due to its low cost and abundance [8], followed by graphene nanoplatelets (GNP) [9] and transition metal dichalcogenides, e.g. tungsten disulphide (WS_2) [10,11] and molybdenum disulphide (MoS_2) [12,13]. Adding these solid lubricants into the metal matrix enables a self-regulated continuous supply during contact, thus can achieve self-lubrication [14]. WS_2 as a transition metal dichalcogenides, provides outstanding anti-wear properties due to the affinity of sulphur to the metal surface [5,15], which improves the interfacial bonding between the additive and metal matrix, in contrast to graphite and GNP that suffer low wettability with aluminium, which often causes agglomeration and poor structural homogeneity [16].

Laser powder bed fusion (LPBF), also known as selective laser melting (SLM), is an additive manufacturing (AM) technique, which selectively melts and consolidates metal powder using a laser beam based on a pre-designed computer-aided-design (CAD) model. Compared with conventional methods like casting and powder metallurgy, LPBF offers unmatched design freedom, time efficiency and feedstock recyclability [17]. The research on Al MMCs with enhanced tribological performances manufactured by LPBF had been focused on those reinforced with wear-resistant additives, such as Al_2O_3 [18,19] and SiC [20], while self-lubricating additives have been investigated in very few studies, limited to graphene [15,21]. More conventionally, spark plasma sintering (SPS) had been used to fabricate Al-WS_2 composites. Rengifo [11] asserted that Al-2 vol% WS_2 exhibits decreased coefficient of friction (COF) compared to pure Al, and the lubricating effect is more prominent at 200 °C than at room temperature. Vaziri et al. [22] reported that among the Al composites incorporating various fractions (1-16 vol%) of WS_2, wear and friction reduced significantly with low WS_2 contents but the effectiveness diminished with higher volume fractions. Although SPS is known to promote in-situ reactions between the constituents of a composite material, and the formation of new compounds between metals and transition metal chalcogenides has been proven to be thermodynamically favourable [23,24], the reactions between Al and WS_2 are yet to be investigated.

To the authors' knowledge, there are no studies in the literature to date that probed LPBF processibility of Al-metal dichalcogenides composites or investigated the interfacial reactions between Al and WS_2 under either LPBF or SPS conditions. This paper aims to develop an understanding of the fabrication of self-lubricating materials by additive manufacturing for green tribological applications and compare their performance with the existing common technique, SPS, as well as shedding the light on the metallurgical reactions involved during processing. This study advances the utilisation of additive manufacturing techniques for tribological applications of Al parts, such as engine blocks, pistons, brake disks, and callipers in the automotive sector and beyond. The effect of WS_2 on the LPBF processability of pure Al parts is explored, and the response of the feedstock material to the fabrication process is analysed. Furthermore, a new methodology for analysing the wear track evolution during friction is proposed. Detailed characterisations of the resultant tribological performance are presented not only quantitatively but also qualitatively during the wear process by evaluating the evolution of the tribo-layer on the wear tracks of the Al-based composites manufactured by both techniques.

2. Material and methods

2.1. Materials

Aluminium powder (purity 99.5%) was acquired from GoodFellow (UK). The self-lubricating additive WS_2 powder (purity 99%) was supplied by Sigma-Aldrich (UK). The Al powder was mixed with 5- wt% WS_2 using the ultrasonic mixing method, following the work in [25]. The WS_2 weight ratio was 5% since 1) it yielded better processability by LPBF in our internal parametric studies compared to other content fractions and 2) this content in the composites prepared by SPS was reported to be effective in lubrication [11]. For the mix, WS_2 was first dispersed in ethanol with the assistance of an ultrasonic probe for 1 h prior to blending. After that, the Al powder was added with vigorous stirring at a temperature of 70 °C (using a hot plate) until the mixture reached a semi-dry state. The slurry was then dried in an oven for 12 h. All powder batches were sieved to 75 μm before processing.

2.2. Fabrication of Al-WS_2 composite

Al and Al-5 wt%WS_2 powder were used as feedstock materials for LPBF and SPS. LPBF processing was conducted using a Realizer SLM50® system, equipped with an yttrium fibre laser with a maximum power of 100 Watts. The specimens were built under an argon atmosphere with an oxygen content under 0.5%, which is the common practice in this system [26] and has not been shown to contribute to detectable oxygen pick-up during processing. The build-plate was maintained at 200 °C to minimize warping during cooling due to non-uniform thermal expansion. A parametric study was conducted by printing cubic samples of 5 mm edge dimension using the process parameters listed in Table 1, at fixed hatch spacing (0.05 mm) and layer thickness (0.04 mm). The three scan strategies in Fig. S1a-c (single, re-melt, and cross-fill, respectively, Supplementary material) were employed, as listed in Table 1, and the samples were named LPBF 1–9 according to the parameter set applied.

SPS was performed by AGUS SPS-630Sx using 13 mm diameter cylindrical graphite dies with pulsed direct current in vacuum (<1

Table 1
Laser scan parameter sets for the samples produced by LPBF.

Parameter set	Scan speed (mm·s^{-1})	Scan strategy	First scan power (w)	Second scan power (w)	Al-WS$_2$ Part processible?
1	250	single	100	–	N
2	500				Y
3	750				N
4	250	Re-melt	50	100	N
5	500				Y
6	750				Y
7	250	Cross-fill			N
8	500				Y
9	750				Y

Pa). Pressure and temperature variation during sintering were pre-programmed. The die was filled with 1.5 g of powder before processing. The consolidation was performed in several continuous stages using the method described in Table S1 (Supplementary material) with the highest temperature of 580 °C and pressure of 50 MPa. The pressure was firstly applied without heating to facilitate the escape of gas between powder particles before sintering.

2.3. Densification and metallurgy characterisation

The density of the fabricated samples was determined by Archimedes' method using distilled water as the liquid for immersion. All specimens were analysed from three repeats for statistical confidence. The feedstock material (Al powder) and bulk specimens were cross-sectioned and polished following the standard metallographic protocols for characterisation. Chemical composition and phase identification were carried out using X-ray Diffraction (XRD) by a Bruker D8 Advance with Cu-Kα X-ray beam source. Two-theta scanning was performed from 10 to 70° with a speed of 0.05 degrees per second. The feedstock material, fabricated specimens, and wear tracks after the tribological test were characterised using an FEI 650 Quanta scanning electron microscope (SEM) equipped with a tungsten filament source and a Hitachi TM3030 scanning electron microscope. The accelerating voltage was set at 15 kV, the micrographs were imaged using the backscatter electron (BSE) detector, and the elemental distribution information was obtained by Energy-dispersive X-ray (EDX) analysis. The microstructure and crystallographic texture of both the cross-sectioned powder and processed parts were studied using electron backscattered diffraction (EBSD). A xenon plasma focused ion beam (FIB), Helios G4 Xe$^+$ pFIB (Thermofisher scientific formally FEI) equipped with a symmetry EBSD and Ultim Max 170 EDX detectors (Oxford instruments) was utilised for the collection of EBSD data and preparation of the transmission electron microscope (TEM) lift-out. EBSD maps were collected at 20 kV, 13 nA. For the heavily deformed fine-grain regions, 10 kV 6.4 nA was used. Kernel average misorientation (KAM) maps were constructed from EBSD data (Kernel size 3x3, max. angle 5°). A standard TEM lift-out procedure was used for sample preparation in the pFIB. TEM experiments were performed with an FEI Tecnai F20 field emission gun scanning transmission electron microscope (FEG-STEM) operated at 200 kV. The TEM was equipped with Oxford Instruments EDX spectroscopy with an 80 cm^2 sized windowless detector. A spot size of 3 and pixel dwell of 3000 μs was used for TEM-EDS data collection. High angle annular darkfield (HAADF) images were recorded along with scanning transmission electron microscope (STEM)-EDS maps. Conventional TEM micrographs were collected with a Gatan Orius camera.

2.4. Hardness and tribological properties characterisation

To evaluate the material's strength, micro-hardness was tested since the intended application of this composite is green tribology, where the material's hardness is directly associated with wear resistance. Nevertheless, micro-hardness testing is a convenient method for assessing a material's strength from small cubic specimens. The microhardness of the samples was measured using a Wilson VH3100 Vickers hardness tester equipped with a diamond pyramid indenter. A load of 0.5 kgf was used for each indentation and the dwell time is set as 10 s. A grid pattern of indentations with an indent-to-indent spacing of 0.5 mm was performed to generate hardness mapping profiles. The corresponding optical micrograph of the indented surface of the LPBF sample across the x-y cross-section (direction definition **Fig. S1d**, Supplementary material) was also obtained by the auxiliary optical lens from the hardness tester. In preparation for tribology testing, all specimens were ground with 400–4000-grit SiC papers, followed by polishing. The tests were conducted using an Anton Paar TRB^3 tribometer according to ASTM G133-05 standard [27] utilising ball-on-flat sliding mode at room temperature without an external lubricant. The normal load, linear motion frequency, and scar length were set at 4 N, 1.5 Hz, and 5 mm, respectively. A 6.35 mm diameter Si$_3$N$_4$ ball was used as the counterpart material for sliding. The COF value of each cycle was recorded, and the wear loss was characterised gravimetrically by the specific wear rate, W, (mm^{3}N^{-1}m^{-1}), which is defined as:

$$W = m/(\rho \cdot L \cdot F) \tag{1}$$

where m is the weight loss (g), ρ is the material density (g/mm^3), L is the sliding distance (m), and F is the normal load (N) applied during the test. The 4000-cycle-average COF is reported based on the mean value of three runs. The analysis of the tribo-film evolution during sliding wear and its impact on friction behaviour was carried out by characterising the worn surface of samples periodically during sliding wear. The sliding wear test was paused after each 500-cycle and the sample was temporarily removed for analysis, after which the test resumed. This process was repeated until 4000 cycles. The test may be paused earlier if obvious COF fluctuation was detected for the observation of tribo-film destruction. Before each intermittent analysis, the sample surface was cooled to room temperature before resuming the test. Optical microscope imaging of the wear tracks was performed using a Nikon Metallurgical Microscope (OPTIPHOT). Dark-field mode was used to acquire the best image quality of the wear track morphology to compare to the unworn smooth surface.

3. Results and discussion

3.1. Ultrasonic mixing of Al-WS$_2$ composite powder

The pure Al powder had an irregular morphology with elongated particles under 100 μm with some satellites (Fig. 1a). The WS$_2$ powder was in the form of agglomerates of flake-shaped particles (Fig. 1b), sticking together by Van der Waals forces; the hexagonal structure of the individual flakes due to the trigonal

prismatic arrangement of WS$_2$ can be seen in Fig. 1c. The sizes of the individual flakes varied from several hundred nanometres to a few microns. After mixing in ethanol, the mixed Al-WS$_2$ powder exhibited a relatively homogenous distribution. Smaller WS$_2$ particles were satellited on the surface of the larger Al particles with some visible small-scale agglomerates of WS$_2$ (Fig. 1d and e). On the other hand, as expected, the morphology of the Al particles after mixing remained unchanged. This is advantageous compared to other works in the literature where mixing techniques involving severe plastic deformation, such as ball milling [28] that led to fracturing and cold welding, promoting unfavoured morphologies. Spherical shaped particles offer better flowability and packing density, which is crucial for LPBF [28,29]. The preservation of the original powder shape using the described ultrasonic mixing strategy makes it a more desirable route for feedstock preparation for in-situ alloying in LPBF.

3.2. Processibility and densification of Al-WS$_2$ composite

In agreement with studies in the literature [28], processing pure Al using LPBF in this study was proven unsuccessful within the parameters' window investigated (Table 1) due to the material's low laser absorptivity [30]. Some cubic samples were successfully manufactured after the addition of 5 wt% WS$_2$ (LPBF-2, 5, 6, 8 and 9, in Table 1). Thereby, it can be asserted that WS$_2$ significantly enhanced the processability due to the improved melt efficiency through the WS$_2$ attached to Al particles, thanks to the successful energy transfer from the former to the latter. A similar strategy was applied by Aboulkhair et al. [28] who introduced 2 wt% CNT to the pure Al feedstock and improved the processability in terms of producing bulk samples. As shown in Table 1, all Al-WS$_2$ specimens using the 250 mm/s scan speed (LPBF-1, 4, and 7) failed due to surface irregularities [31] that obstructed the re-coater, interrupting the build process. Similarly, increasing the scan speed to 750 mm/s with a single scan strategy (LPBF-3) was unsuccessful, which was attributed to the poor wetting of the melt that resulted in balling [31].

Fig. 2a summarises the relative density values of the LPBF and SPS specimens. The SPS Al and SPS Al-WS$_2$ showed higher relative density values of 99.9 ± 0.1% and 99.6 ± 0.2%, respectively, compared to the LPBF parts. SPS is known as a technique that can process Al parts with relatively high density due to the direct electric discharge, which generates plasma between the particle gaps and breaks the oxide layer on the surface [32], promoting the sintering of the particles to consolidation thanks to the pressure and temperature combination. In contrast, LPBF of Al parts, particularly pure Al, typically suffer from extensive porosity due to the material's physical properties (poor flowability, high reflectivity in the wavelength range used in the process) that compromise melting efficiency during the process [33]. As expected, the porosity content in the LPBF samples varied with the process parameters. Significant reduction in porosity was observed when using the pre-sinter strategy (LPBF-5, 6, 8, and 9). The preliminary lower-power scan before the full-power scan served as an in-situ drying stage, which decreases the moisture content and thus drastically reduces porosity [34]. To further study the porosity features of LPBF parts, optical microscopy was performed on the x-y cross-section of LPBF parts, i.e. perpendicular to the building direction. According to the forming mechanism, pores are categorised as metallurgical, lack-of-fusion, and keyhole pores [34,35]. At 500 mm/s, the sample LPBF-2 (Fig. 2b) showed all three types of porosity, yielding the lowest density. Fixing the scan speed at 500 mm/s and changing the scan strategy to re-melt (LPBF-5), the larger pores were eliminated, and small metallurgical pores became the major defect (Fig. 2c). Quantitatively, the density was significantly improved. When the scan speed increased from 500 mm/s to 750 mm/s (LPBF-6), the content of metallurgical pores was reduced, but lack-of-fusion pores formed due to insufficient laser energy density for material fusion between the scan tracks [31] (Fig. 2d), causing a slight decrease in the density. When the cross-fill pattern was employed instead of re-melt, a further increase in relative density was observed, especially at the 750 mm/s scan speed since the reduction in the lack-of-fusion pores was significant (Fig. 2f). This scan strategy is also beneficial for the mitigation of anisotropy
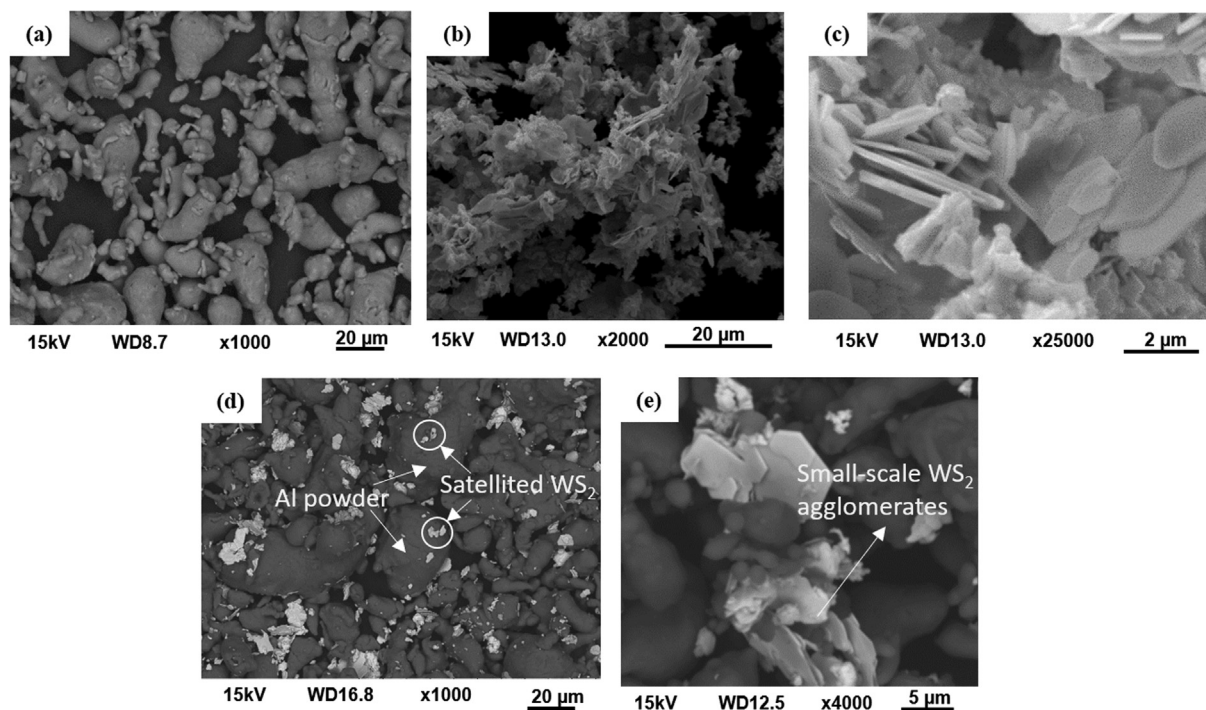

Fig. 1. SEM images of the starting powders used in this study. (a) pure Al; (b) and (c) WS$_2$ particles; (d) and (e) ultrasonic mixed Al-5 wt%WS$_2$ powder.
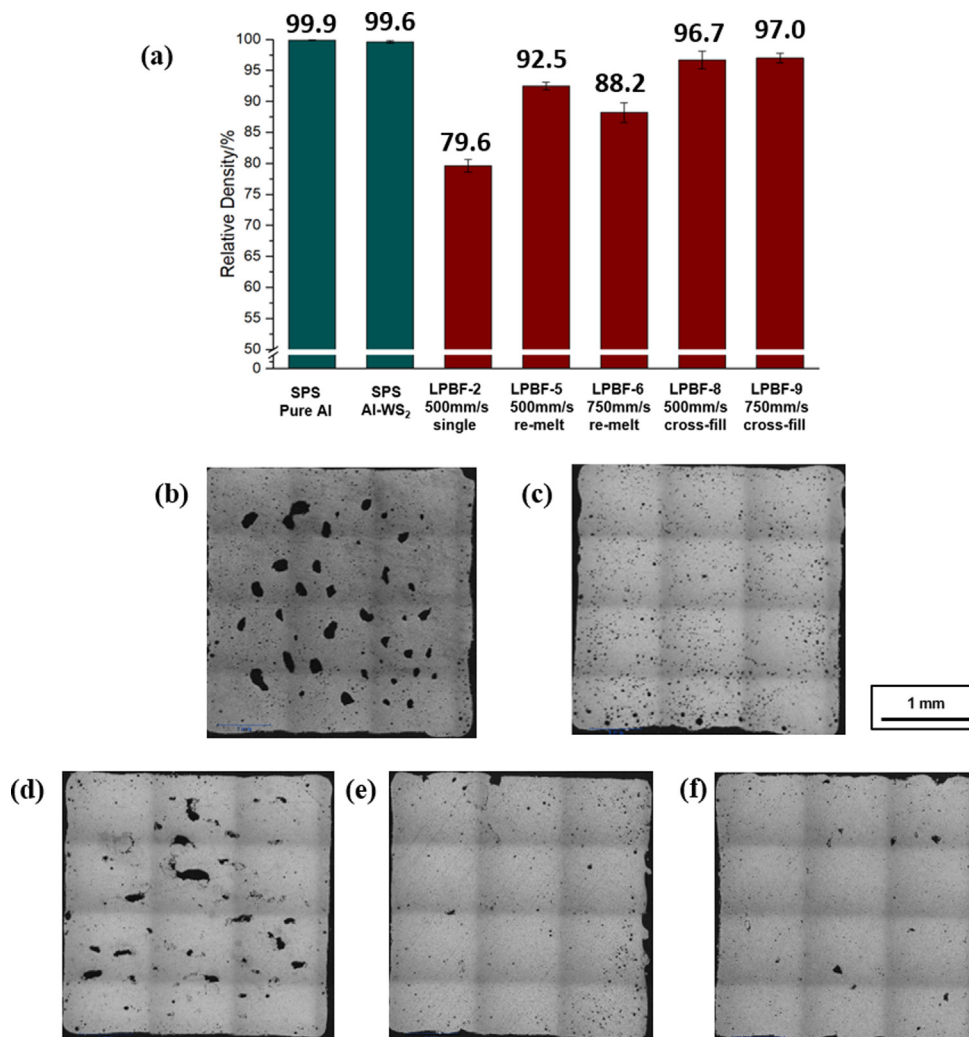
Fig. 2. Relative density of SPS and LPBF parts and images showing LPBF surface porosity. (a) The relative density of successfully processed samples determined by Archimedes' Method. (b)-(f) Porosity of LPBF Al-WS$_2$ parts using different scan parameter sets illustrated by optical microscope images on the x-y cross-section: (b) LPBF-2 (500 mm/s Single); (c) LPBF-5 (500 mm/s re-melt); (d) LPBF-6 (750 mm/s re-melt); (e) LPBF-8 (500 mm/s cross-fill); (f) LPBF-9 (750 mm/s cross-fill).

through altering the scan direction using cross-fill since the second scan that rotated 90°facilitated fusing the gaps that formed with the first scan.

3.3. Metallurgy of LPBF and SPS Al-WS$_2$ composites

Since the LPBF-9 samples yielded the highest relative density (97.0 ± 0.9%), these were selected for characterisation (referred to from this point onwards as "LPBF Al-WS$_2$") and comparison with SPS specimens. Fig. 3a shows the XRD patterns of the mixed powder, LPBF Al-WS$_2$, SPS Al and SPS Al-WS$_2$. The mixed powder showed strong characteristic peaks corresponding to Al (PDF#89-4037) and 2H-WS$_2$ (PDF#87-2417). The main characteristic peak of WS$_2$ located at $2\theta = 14.3°$ (0 0 2) remained after both LPBF and SPS processing but with a much weaker intensity, confirming the retention of some hexagonal structure after either sintering or laser scanning. The potential reason for this lower intensity is the smaller fraction of crystalline WS$_2$, which will be discussed later. As expected, the pattern for SPS pure Al samples showed only the characteristic peaks for Al. Regarding the SPS Al-WS$_2$ samples, peaks corresponding to Al$_{12}$W (PDF#65-1786) were detected. Also, the pattern revealed the existence of a crystal structure that matches the Bravais lattice of Al$_5$Mo (rhombohedral, R-3c, Fig. 3b, PDF#65-7143) but does not correspond to the lattice

parameters of Al$_5$W (hexagonal, P63, PDF#30-0046) in the database. Multiple alloy phases can co-exist for the Al-W binary system, which may result in various correspondent peaks for the Al-W alloy after processing [36,37]. Note that both rhombohedral (R-3c) and hexagonal (P63/mmc) are the possible lattice structures for intermetallic compounds formed by different processing conditions [38,39]. Since W and Mo are transition metals from the same subgroup and have plenty of compounds sharing the identical lattice structure, such as Mo and W, MoS$_2$ and WS$_2$, Al$_{12}$Mo and Al$_{12}$W, it is postulated that these peaks (marked as "*" in Fig. 3a) are attributed to the formation of Al$_5$W during SPS. Regarding LPBF Al-WS$_2$, apart from Al and WS$_2$, the XRD patterns also showed the characteristic peak of W (PDF#89-2767) at $2\theta = 40.3°$ (1 1 0) with no apparent signals for Al-W intermetallic phases.

The distribution of WS$_2$ in the LPBF composite samples can be observed in the SEM images in Fig. 4a and b, showing no large-scale clustering, unlike the starting powder. Instead, nanosized particles mainly segregated at the boundaries of the melt pools (Fig. 4a, red dash lines), which is commonly observed for particle reinforced LPBF composites [28]. The good dispersion of the reinforcements can be due to the Marangoni flow within the melt pool that dispersed the clusters and assisted in mixing the reinforcements throughout the matrix [21]. These nanosized particles show high contrast compared to the Al matrix in the TEM micrograph in
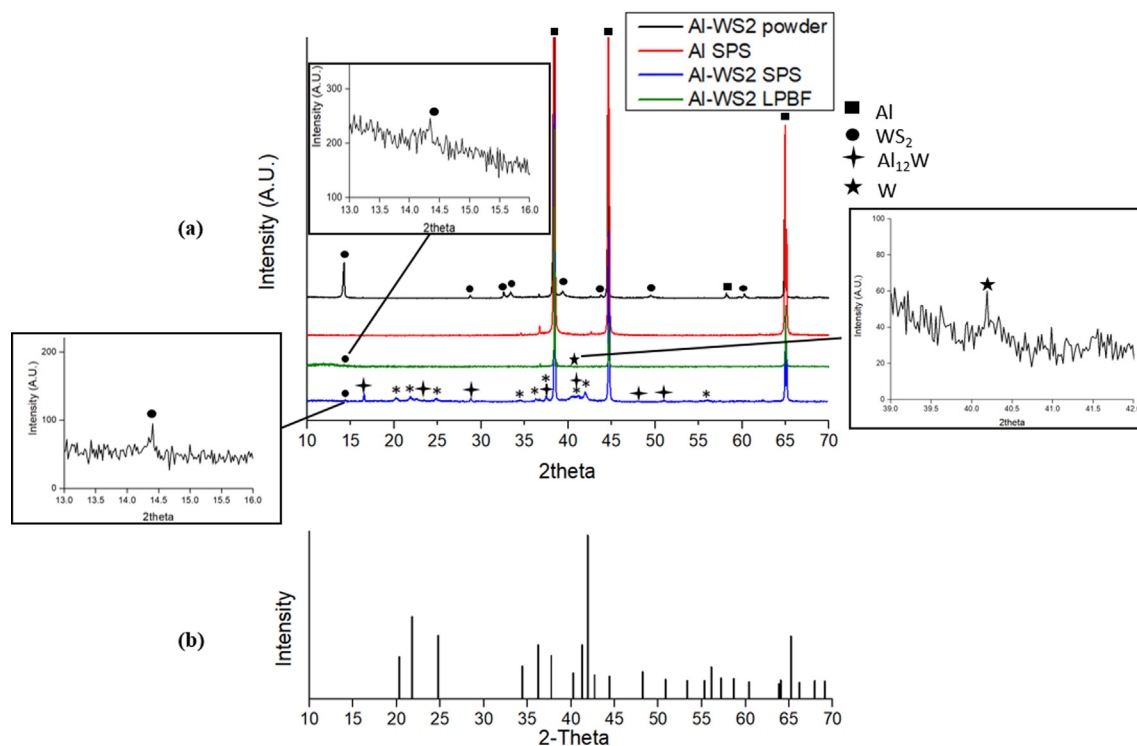
Fig. 3. XRD patterns of different parts. (a) Al-WS$_2$ mixed powder, SPS, or LPBF processed parts; (b) Al$_5$Mo from database [PDF#65-7143, marked as "*" in (a)].

Fig. 4c. EDX spectrum on these particles showed an atomic ratio of about 1:2 for W:S (Fig. 4d, the Cu in the spectra is from the TEM grids), suggesting that these are refined WS$_2$. This is further supported by the area highlighted by white circles in Fig. 4c and e, where the Al signal diminished, but W and S signals accumulated. Furthermore, there are also regions on the map where S and W were detected separately (Fig. 4c and e, yellow circles), indicating the presence of elemental S and W or Al-W compound. The decomposition of WS$_2$ content into W and S during laser processing (laser cladding) has been reported by several studies previously [40,41].

It should be noted that the distribution of the reinforcements throughout the Al matrix was not homogeneous as both reinforcement-rich (Fig. 4a) and reinforcement-sparse (Fig. 4b) regions were detected. Random particles with sizes similar to the WS$_2$ feedstock material, i.e. about 1–2 μm, were observed in the reinforcement-sparse regions mainly but also occasionally in the reinforcement-rich region (Fig. 4a and b, marked with white circles). An example of these micro-particles in the matrix is Fig. 5a, with the selected area diffraction pattern (SADP) of the Al matrix and the particle shown in Fig. 5e and f, respectively. According to the SADP pattern, the particle matched the crystal structure of W, in agreement with the EDX results (Fig. 5b). These findings, combined with the W peak seen in the XRD pattern of the LPBF sample (Fig. 3a), are evidence for the formation of micro-W through decomposition of the WS$_2$ as a result of the laser-material interaction, which agrees with the findings of Wang et al. [41]. These W particles may be transformed from WS$_2$ large flakes or clusters, of which the Marangoni flow was not strong enough to break the Van de Waal force. Interestingly, TEM also revealed some petal-like grey features surrounding the W micro-particles (Fig. 5a). Chemical analysis in Fig. 5b indicated that these features are in-situ formed Al-W intermetallics. Similar microstructure was reported for an LPBF Al-W composite [36], which were believed to provide high strength for the material, but the fraction of the intermetallic phase was relatively low in the current study due to the lower starting W content, given that

their source is the decomposition of WS$_2$. Therefore, it can be concluded that the nanosized WS$_2$ particles locally and partially decomposed as per: WS$_2$ → W + 2S, while the larger WS$_2$ flakes or clusters transformed into W micro-particles in addition to Al-W intermetallics forming at the W-Al interface as per: Al + W → Al$_x$W.

The reinforcements in the SPS Al-WS$_2$, on the other hand, were scattered in the matrix in the form of clusters showing as brighter phases in contrast to the darker Al matrix (Fig. 6a). As seen in higher magnification (Fig. 6b), except for Al matrix and WS$_2$ phase, a shell structure (red arrow) had in-situ formed at the interface, which can be related to the intermetallic peaks observed XRD pattern for the SPS composite (Fig. 3a). Fig. 6c shows an STEM micrograph of the interfacial feature along with EDX maps (Fig. 6d) where the WS$_2$-intermetallic-Al structure was clearly identified. An oxide layer separated the WS$_2$ and the intermetallic phase. Since the SPS was performed under vacuum, this layer should pre-exist between Al and WS$_2$, meaning the WS$_2$ permeated into Al matrix and promoted the reaction. The higher magnification image in Fig. 6e reveals the microstructure of the intermetallic shell with noticeable contrast. Elemental analysis (Fig. 6f) suggested that W and S distributed separately, with the brighter region comprising the Al-W intermetallic and the darker region possibly containing Al$_2$S$_3$ and some oxides.

According to the atomic layers appearing in the high-resolution TEM (HRTEM) image of SPS Al-WS$_2$, the phases in the shell were arranged with preferred orientations surrounding the WS$_2$ core (Fig. 7a, straight-line directions). Two sorts of layer spacings were found, which corresponded to the atomic arrangement of Al$_5$W (Fig. 7a) and Al$_{12}$W (Fig. 7b). The examples of the SADP of WS$_2$ core region and the intermetallic phases are provided in Fig. 7d and e, respectively. Previous studies showed that Al-W compound exhibits much higher strength than Al [42], while WS$_2$ is a solid lubricant with a soft nature. It is thus speculated that the interfacial compound can increase the hardness of the composite besides the tribological advantage of the WS$_2$. It is noteworthy that a sim-
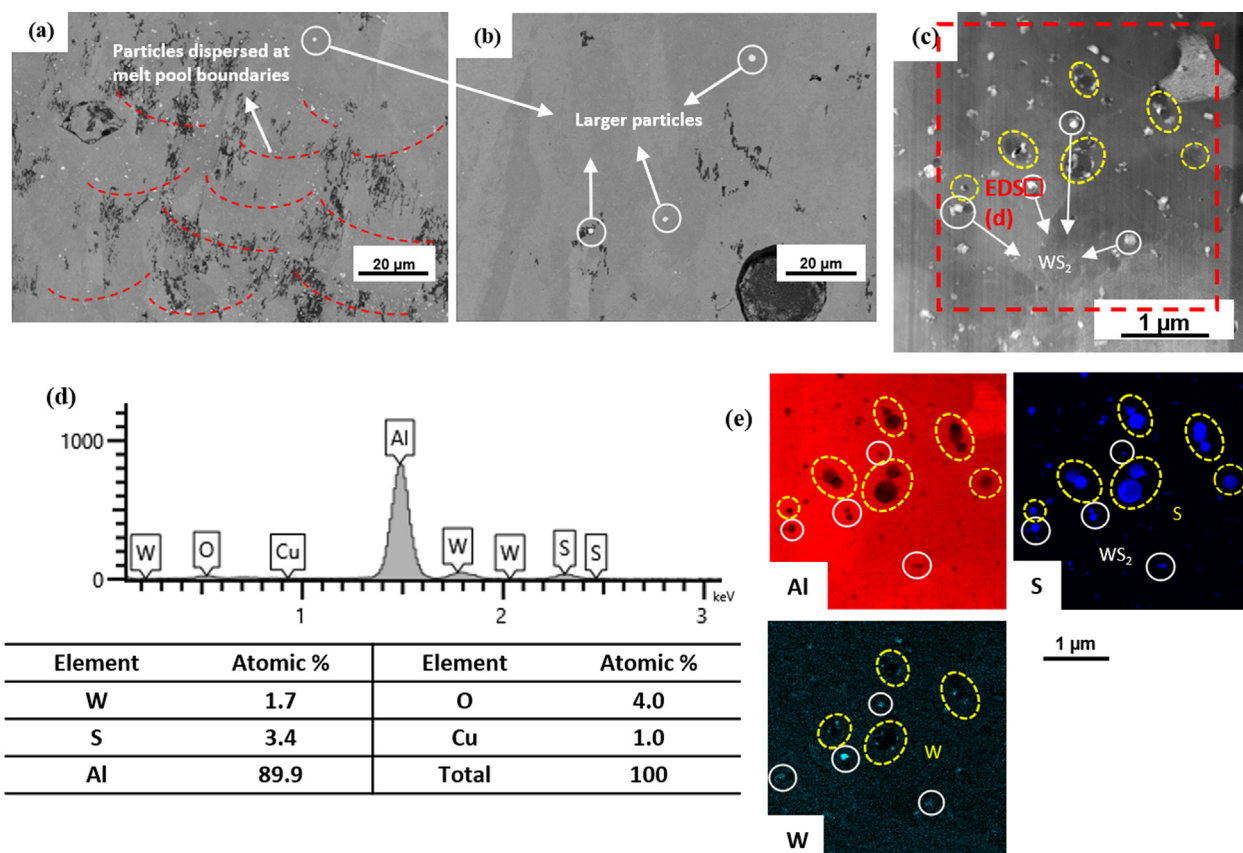
Fig. 4. SEM and STEM images showing the reinforcement phases distribution in LPBF Al-WS$_2$. (a) SEM image showing the distribution of particles in WS$_2$ rich region in the LPBF Al-WS$_2$ sample; (b) SEM image showing the large reinforcement grains in WS$_2$ sparse region; (c) STEM image showing the dispersion of reinforcement phases in Al matrix for LPBF Al-WS$_2$. All images were taken from the vertical cross-section (X-Z plane); (d) EDX spectrum of the selected area in (c) (red rectangular box); (e) EDX maps illustrating the distribution in the dash rectangle area in (c). Colour print required.

ilar metallurgical reaction at the interface during SPS was reported for Cu-WS$_2$ composites [43], in which the authors claimed the formation of Cu$_2$S. The in-situ metallurgical reaction between Al and WS$_2$ during SPS can be therefore speculated as Al + WS$_2 \rightarrow$ Al$_x$W + Al$_2$-S$_3$. However, the present study did not find evidence for the formation of Al$_2$S$_3$ by XRD or TEM diffraction patterns. This can be due to the high moisture sensitivity of Al$_2$S$_3$ when exposed to the atmosphere, which may have led to its hydrolysation that produced H$_2$S, reducing the Al$_2$S$_3$ content [44]. Indeed, the particular odour of H$_2$S was detected during sample preparation, which supports the above inference.

EBSD patterns of both large (tens of microns) and small (few microns) pure Al powder particles in Fig. 8a and b show the polycrystalline structure with random orientations. The grains with similar orientations were locally separated by low angle grain boundaries formed of nanocrystalline domains. After LPBF processing, the Al grain morphology changed significantly compared to the original powder. In the former, the elongated Al grains, following the direction of the thermal gradient, can be seen in the inverse pole figure (IPF) in Fig. 8c, which is a typical feature of LPBF materials [28]. Since no alloying elements were involved during solidification, the constitutional supercooling had been hindered. Combined with the high thermal conductivity of Al and high solidification rate associated with the process, the grain growth was aligned along the heat dissipation direction and eventually resulted in such columnar morphology. In the SPS samples, some nanocrystalline grains from the starting powder were retained and the grain morphologies resembled the random orientations observed in the starting powder because of the limited grain

growth during the rapid sintering process (Fig. 8d and e). The introduction of WS$_2$ into the matrix increased the zero-solution area in the IPF map since the WS$_2$ particles posed challenges in sample preparation for EBSD characterisation. However, the overall microstructural features were similar to the pure Al samples.

From a texture point of view, according to the literature, it is believed that the high thermal conductivity of Al results in LPBF Al parts adopting no preferential solidification direction, which leads to an overall weak texture [28]. However, the LPBF sample in this study showed a relatively strong ⟨100⟩ texture along the building direction (Z) compared to the SPS samples. This is due to the intrinsic absence of crystallographic texture in the SPS samples, following the randomly oriented structure in the feedstock material. The mean equivalent circle sizes of the grains determined by EBSD were 5 ± 2 for SPS Al, 5 ± 3 for SPS Al-WS$_2$, and 20 ± 15 for LPBF Al-WS$_2$. SPS samples (Al and SPS Al-WS$_2$) exhibited similar grain sizes, indicating the micro-sized WS$_2$ posed no grain refinement on the Al matrix during sintering. In contrast to SPS Al-WS$_2$, LPBF Al-WS$_2$ showed a much larger average grain size as well as the standard deviation. Similar results were reported in the literature for stainless steel [45], although ultra-fine microstructures should have been commonly observed due to the extremely high cooling rates associated with LPBF [46]. Since the SPS process did not alter the original fine polycrystalline structure of the Al powder, it yielded parts with a finer grain structure compared to LPBF, which involved melting and solidifying the material thus altering the microstructure significantly. EBSD patterns from the transverse cross-sections at higher magnification for the LPBF and SPS Al-WS$_2$ parts showed equiaxed grains in the former (Fig. 9a), while the lat-
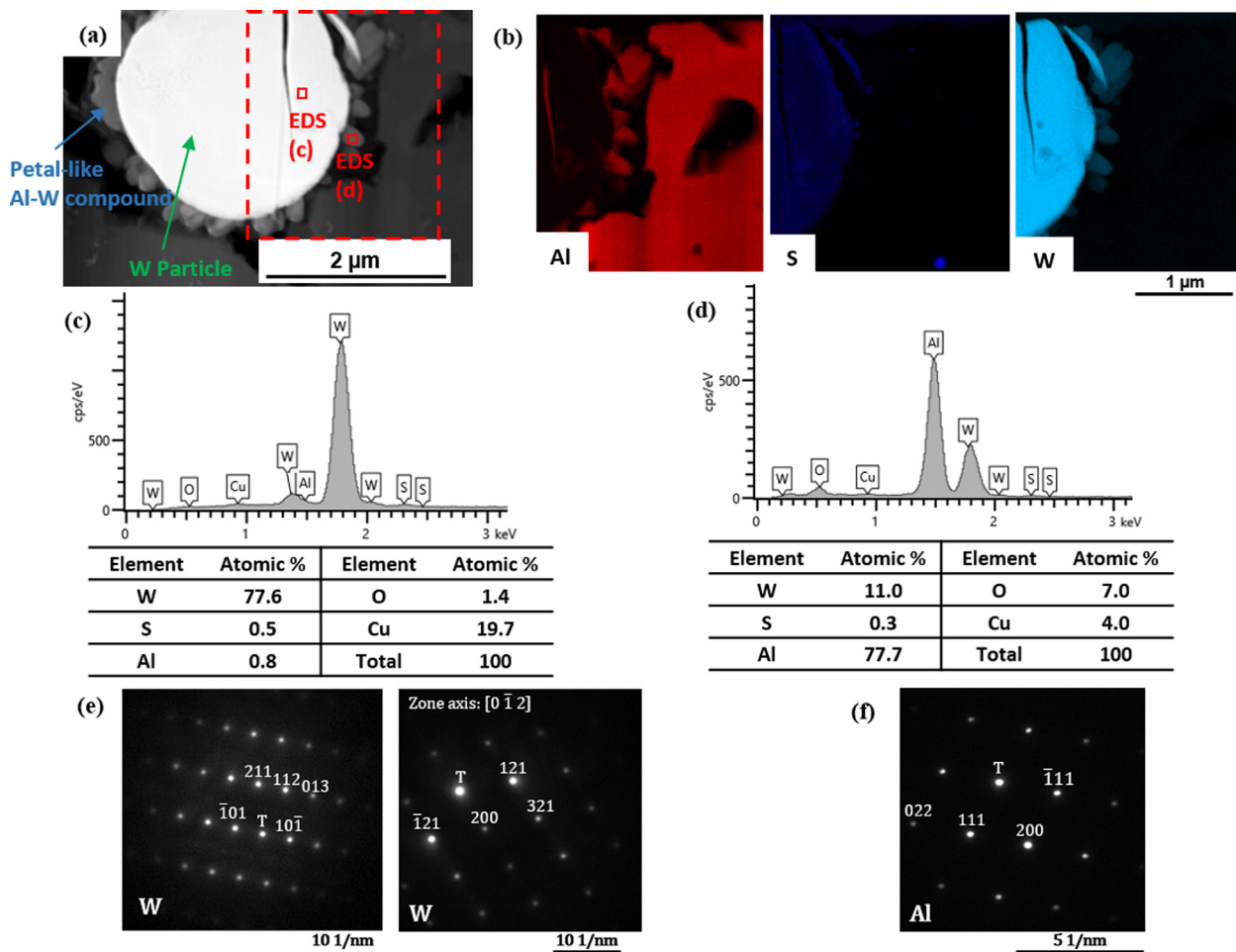
Fig. 5. TEM and EDX analysis on the W particle in the LPBF composite. (a) STEM HADDF images showing an in-situ formed W particle and petal-like Al-W in the matrix; (b) EDX maps illustrating the elemental distribution in the dash rectangle area in (a); (c) and (d) EDX spectra of the selected areas in (a) (red rectangular box); (e) and (f) The SADP for the W particle and Al matrix. Colour print required.

ter (Fig. 9c) did not manifest a noticeable difference compared to the longitudinal plane. The zero-solution areas (annotated by the white circles) for the SPS part in Fig. 9 (c) and (d) should be WS_2, as confirmed by the EDX maps showing the location of S and W in Fig. 9 (e) and (f), respectively. The KAM maps illustrated that dense dislocations forests and networks were randomly detected in the LPBF samples in Fig. 9b. On the other hand, relatively high KAM values (i.e., high misorientation level) were concentrated near the grain boundaries and where smaller grains were located in the SPS samples in Fig. 9d. Despite the larger grain size in the LPBF samples, the average KAM value determined by EBSD was 1.23° for LPBF Al-WS_2 vs. 0.72° for SPS Al-WS_2, indicating a higher local dislocation density within the LPBF part. This is attributed to the distinctive experiences the material being processed goes through during manufacture using the two fabrication techniques. During SPS, the feedstock material is consolidated without melting, therefore no significant changes occur to the misorientation level and structure of grains during fabrication [45]. On the other hand, being classed as a melting-based manufacturing process, materials processed by LPBF experience rapid solidification from the melt with the solidification rates estimated to be in the order of 10^{-6} K m^{-1} [46], which means that the grain structure in the starting feedstock material is completely wiped away and replaced by the LPBF microstructure of sub-cells with high degree of residual stress [28].

3.4. Hardness and tribological analysis of LPBF and SPS Al-WS_2 composite

The micro-hardness and tribological properties of LPBF and SPS Al-WS_2 are summarised in Table 2. The hardness profile across the X-Y plane for LPBF and SPS samples along with the respective mean hardness values are presented in Fig. 10. The LPBF Al-WS_2 sample exhibited higher average micro-hardness than both SPS parts despite the higher porosity content. This can be attributed to two distinctive strengthening factors. The first is the decomposition of the WS_2 and its reaction with the Al matrix upon laser irradiation forming W (a harder phase), as evidenced by the reduction of its main peak intensity in the XRD pattern in Fig. 3a. The second is the higher dislocation density introduced into material during LPBF [28,47], as determined by the average KAM value in EBSD (Fig. 9) due to rapid solidification. Besides, the LPBF sample also displayed more scatter in the data, i.e. higher standard deviation. The large spatial variation in hardness is common in LPBF parts [18], which is linked to the random porosity since the regions in the vicinity of a pore are typically softer.

The SPS Al sample presented the lowest average hardness and standard deviation. A slight increase in hardness was recorded for the SPS composite with some special variations due to reinforcement clustering. The increase in hardness by adding WS_2 to an Al matrix using various production routes, including SPS, agrees
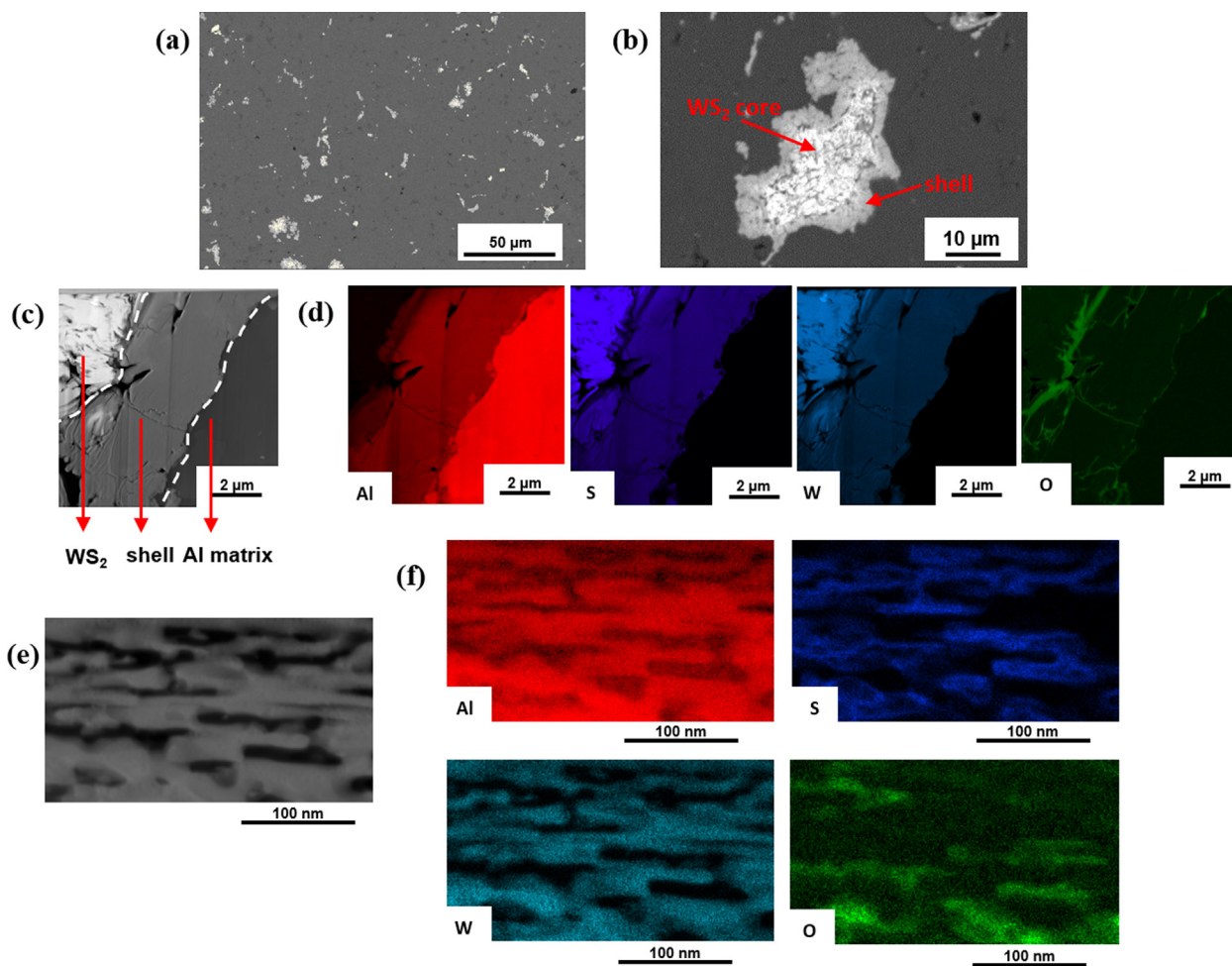
Fig. 6. SEM and STEM images showing the phase presented in the SPS Al-WS$_2$: (a) low magnification SEM image showing the distribution of WS$_2$ phases; (b) SEM high magnification imaging showing the core–shell structure of the WS2 phase in SPS Al-WS$_2$. (c) STEM HAADF image showing the microstructure of the interfacial region in SPS Al-WS$_2$; (d) EDX map showing the elemental distribution in (c). (e) STEM HAADF image showing the microstructure of the intermetallic shell in SPS Al-WS$_2$; (f) EDX map showing the elemental distribution in (e). Colour print required.

with the literature [10,11,22]. It should be, however, noted that WS$_2$ itself is only a solid lubricant with soft nature [48]. Since the WS$_2$ used in all quoted studies were nano-sized, a common explanation for the strengthening mechanism is that the WS$_2$ located along the grain boundaries of the Al matrix played a pinning role and impeding the dislocations' motion [10,11]. Whereas the micro-sized WS$_2$ powder used in this study did not promote grain refinement, as EBSD analysis confirmed. On the other hand, since the in-situ formed Al-W compound possesses much higher strength than Al [42], it is thus speculated that the formation of the harder interfacial compound is the major contributor to the strengthening mechanism.

Independent of the manufacturing route, the Al-WS$_2$ composite samples yielded enhanced tribological properties compared to the SPS Al, as shown in Table 2. This is because the formation of new phases increased the hardness and the material's wear resistance positively correlates to hardness, while the WS$_2$ served as the solid lubricant that reduced COF. Also, the LPBF Al-WS$_2$ specimen exhibited a slight reduction on both average COF and wear rate compared to SPS Al-WS$_2$. The reason will be discussed later. The friction behaviour of both SPS and LPBF samples involved a fluctuation stage and stabilised stage (Fig. 11a). The optical micrographs of the wear tracks after each 500 cycles are shown in Fig. 11b with the zoomed-in micrographs provided in **Fig. S2** (Supplementary material).

During the fluctuation stage, a high COF value and fluctuation were observed due to the asperities in contact, which corresponded to the bright wear tracks at the first 500 cycles for all samples (Fig. 11b). At this stage, an unstable tribo-layer with high hardness was forming on the contact area. The formation of the tribo-layer (or mechanically-mixed layer, MML [49]) is associated with plastic deformation and the reaction between the worn material and oxygen during sliding wear, which resulted in a darker region on the area of contact [10]. However, since the tribo-layer was thin and non-uniform, it went through repetitive cycles of breakdown and reformation. The transition from the initial fluctuation stage to the stabilised stage occurred when a relatively stable tribo-layer formed and subsequently the COF decreased, which was at about 600 cycles for the LPBF samples but more than 1500 cycles for both SPS samples (see Fig. 11a). The earlier formation of a stable tribo-layer for the LPBF parts could be attributed to the higher surface area of the fine reinforcement phase, which detached as debris during wear and readily reacted with Al and oxygen in the atmosphere [10], forming the tribo-layer. This gave rise to the conspicuous difference in the worn surface at 1500 cycles in Fig. 11b, where a uniform tribo-layer had already generated for the LPBF sample, while a brighter surface with non-uniform tribo-layer was still visible on the SPS Al-WS$_2$ sample. On the other hand, it is known that inferior material hardness can cause tribo-layer instability [50], which resulted in nearly no
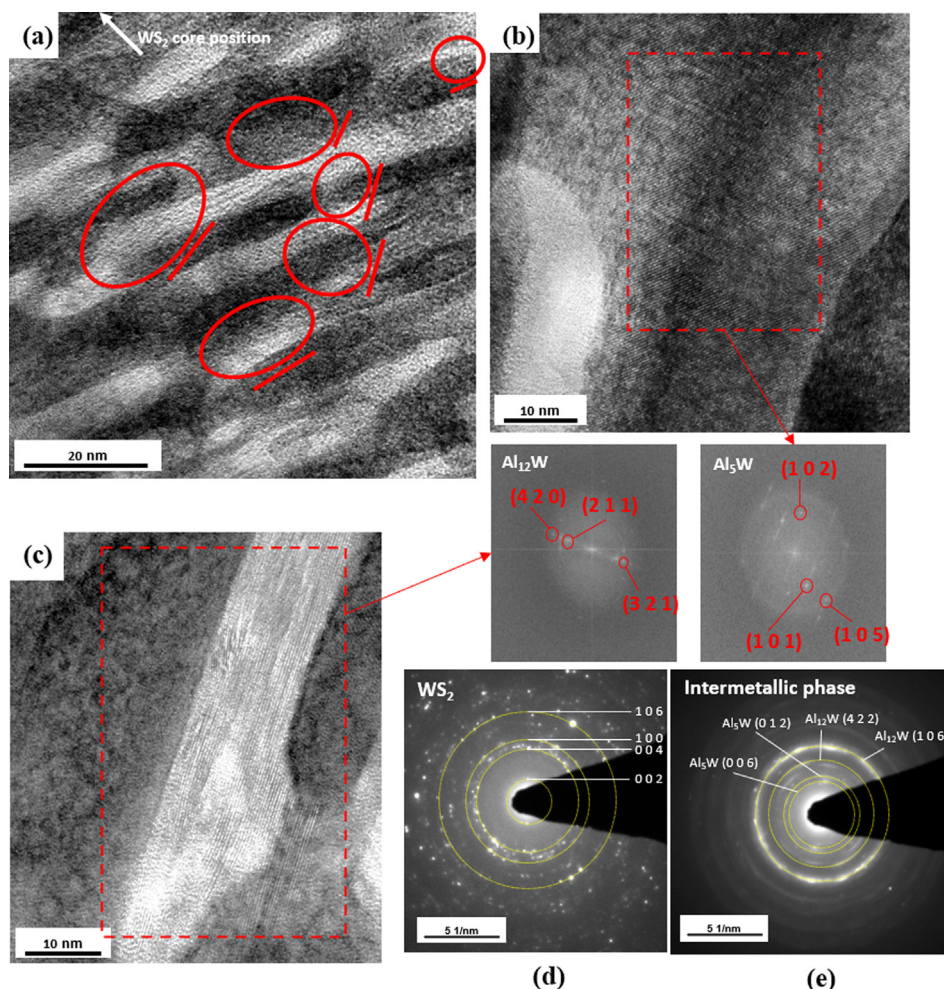
Fig. 7. TEM micrographs revealing the microstructure of the intermetallic phase between WS_2 and Al matrix. (a) HRTEM image showing the intermetallic phase microstructure with crystal planes observed. Red straight lines indicate the crystal plane directions inside the circle; (b) and (c) examples of the region revealing the Al_5W and $Al_{12}W$ crystal structures with the corresponding Fast Fourier transform (FFT) results in the red rectangular area. (d) and (e) examples of the SADP of the WS_2 core and intermetallic phase, respectively.

steady tribo-layer observed on the worn surface of SPS Al at this stage. The earlier formation of a protective tribo-layer in the first stage of friction results in a decrease in the 4000-cycle average COF for LPBF Al-WS_2 compared to the SPS Al-WS_2. This interesting result combined with its higher hardness are evidence for the enhanced wear resistance that can be achieved from this composite material when processed by LPBF.

Table 3 displays the wear volume of the samples after each 1000-cycles of sliding wear. In some cases, the material loss was barely detectable and therefore no data is shown for those. Both SPS and LPBF Al-WS_2 showed lower wear volume than SPS Al, especially after the first 1000-cycles of sliding wear. On the other hand, the wear volume drastically reduced as wear progressed to the stabilised stage, suggesting a transition from severe wear to mild wear. This does not follow the classic Archard's model [51] for theoretical wear prediction, by which the wear volume is expected to rise linearly with increasing sliding distance, since the classic model does not consider the gradual formation or breaking of the tribo-layer during sliding wear [52,53].

The morphology of wear tracks on the samples after various sliding distances can be seen in the SEM images in Fig. 12 with the EDX maps showing the distribution of oxygen. After the first 500 cycles, cracks and plastic deformation were observed on all surfaces (Fig. 12 a, c, and e), which are typical evidence for adhesive wear [53]. Relatively few cracks were detected on the LPBF Al-WS_2 (Fig. 12a), and oxides had formed a non-uniform pattern parallel to the sliding direction (Fig. 12b), indicating that the tribo-layer started to generate at an early stage for the LPBF part. On the other hand, more cracks and plastic deformation were observed for both SPS samples (Fig. 12c), and the oxygen content was merely scattered on the worn surface in the form of oxide clusters, which agrees with the wear track evolution analysis. This is further supported by the atomic ratios of elements on the worn surface concluded in Table 4, in which the oxygen on the worn surface of the LPBF Al-WS_2 was 24.4% compared to only 5.6% and 5.0% for SPS Al-WS_2 and Al. After 4000 cycles, all surfaces became smoother. The worn surfaces of both LPBF and SPS Al-WS_2 showed much higher O content distributed on the surface, indicating the formation of a uniform tribo-layer in the stabilised stage of friction. The surfaces also became smoother, and instead of large cracks, grooves became the main feature of the tracks (Fig. 12d-f), which is a sign of abrasive wear [54]. However, due to the lower hardness, some micro-cracks were introduced on the surface of SPS Al-WS_2 by the ploughing of the Si_3N_4 ball. For SPS Al, in contrast, the oxygen content on the worn surface showed a relatively minor increase after 4000 cycles
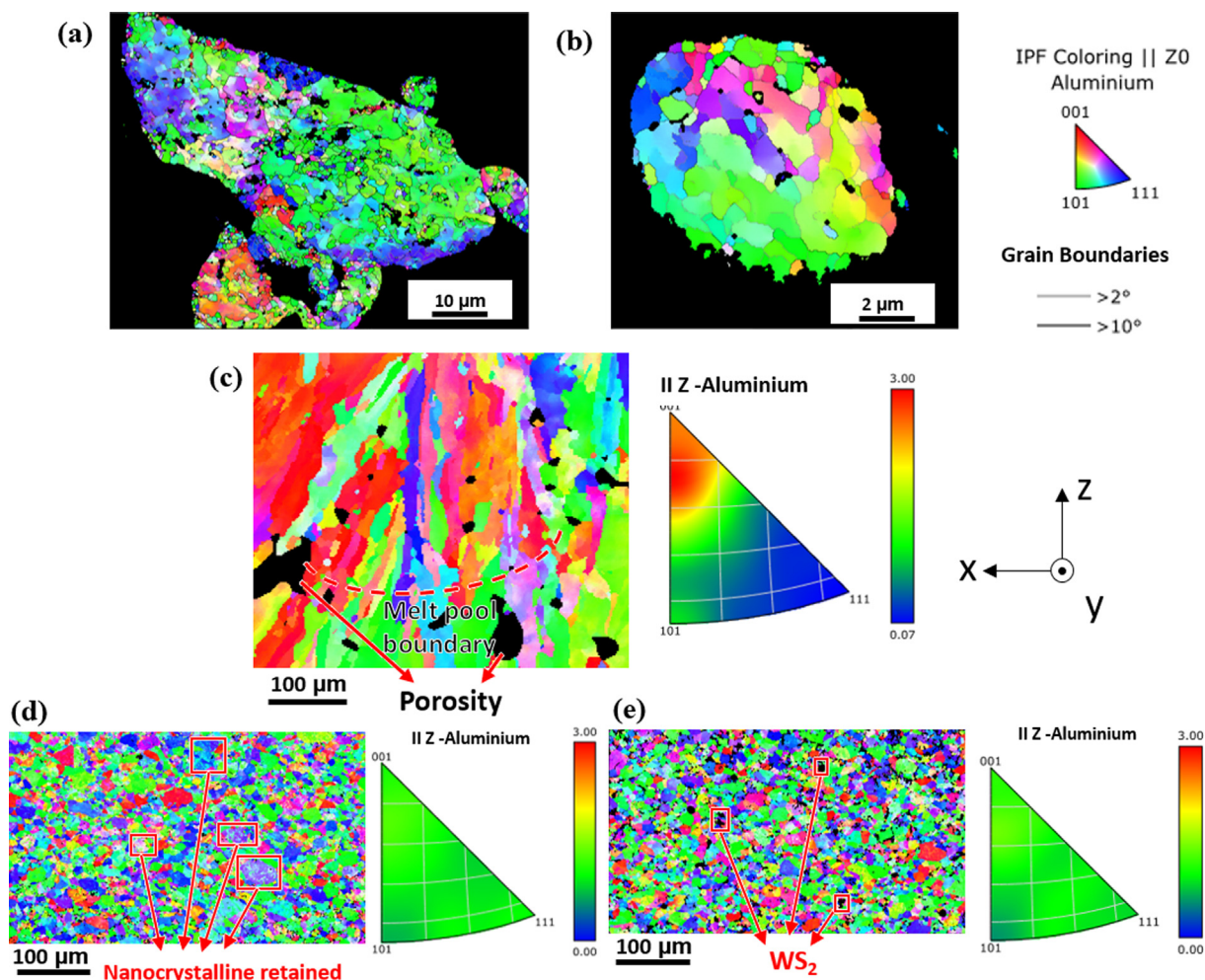
Fig. 8. EBSD results of the Al powder and processed parts. (a) and (b) Examples of IPF maps (0.1 μm step size) of the pure Al powder with two different sizes. The IPF colour maps (2.0 μm step size) and Inverse pole figures of the vertical cross-section of: (c) LPBF Al-WS$_2$; (d) SPS Al; (e) SPS Al-WS$_2$. The definition of sample directions is demonstrated in Fig. S1d and e (Supplementary material). Colour print required.

(Table 4), and the wear track was relatively rough, with more oxide debris randomly dispersed on the surface, meaning that the SPS Al sample did not form a tribo-layer that is homogeneous in the microscale.

The EBSD maps of the cross-sections perpendicular to the worn surfaces after 4000-wear-cycles in Fig. 13 show the effect of sliding wear on the microstructural depth profile of each sample. The wear-affected subsurface of both surfaces consisted of two regions (marked as I and II). The microstructure of SPS parts evolved from refined nanocrystalline near the contact area in region I due to severe plastic deformation, to elongated grains perpendicular to the load direction in region II, and finally to undeformed bulk material (Fig. 13b and c). This transformation of the sub-surface structure was attributed to the stress gradient from the contact area caused by sliding wear, in agreement with the literature [55]. The plastic deformation poses a work hardening effect on the worn surface material, which increases the sub-surface hardness and protects the material underneath. The grain elongation in region II was, however, not observed in the case of the LPBF sample due to the relatively larger starting grain size. Instead, the plastic deformation resulted in an abrupt change in the crystal orientation compared to the material beneath (Fig. 13a, region II) that is similar to the sub-surface of a single-crystal aluminium part after machining [56]. The total wear affected depth was estimated 40 μm for SPS Al

but was reduced to about 35 and 30 μm for SPS and LPBF Al-WS$_2$, respectively, which indicated the inverse relationship between the plastic deformation depth and material wear rate and was in agreement with Gallo et al. [55]. This is due to the relatively high hardness of the LPBF part (Fig. 10), as a more robust and thinner tribo-layer can be formed for the material with higher mechanical strength [50].

4. Conclusions

The Al-WS$_2$ composite feedstock prepared via ultrasonic mixing followed by LPBF was studied for the first time by comparing its microstructure and tribological properties to the SPS counterparts. The feedstock preparation method retained the starting morphology of the powder used, which is advantageous for LPBF powder requirements, showing that this method can be translated to other material systems in the field of materials design for AM, particularly for high throughput screening of new compositions. Exploiting the excellent contact between the WS$_2$ and the Al particles' surfaces enabled successful LPBF processing, compared to pure Al. The LPBF process parameters were optimised to produce near fully dense parts (97.0 ± 0.9%), while SPS parts were fully dense (99.6 ± 0.2%). The microstructure evolution of this composite fabricated by different techniques was also revealed for the first time.
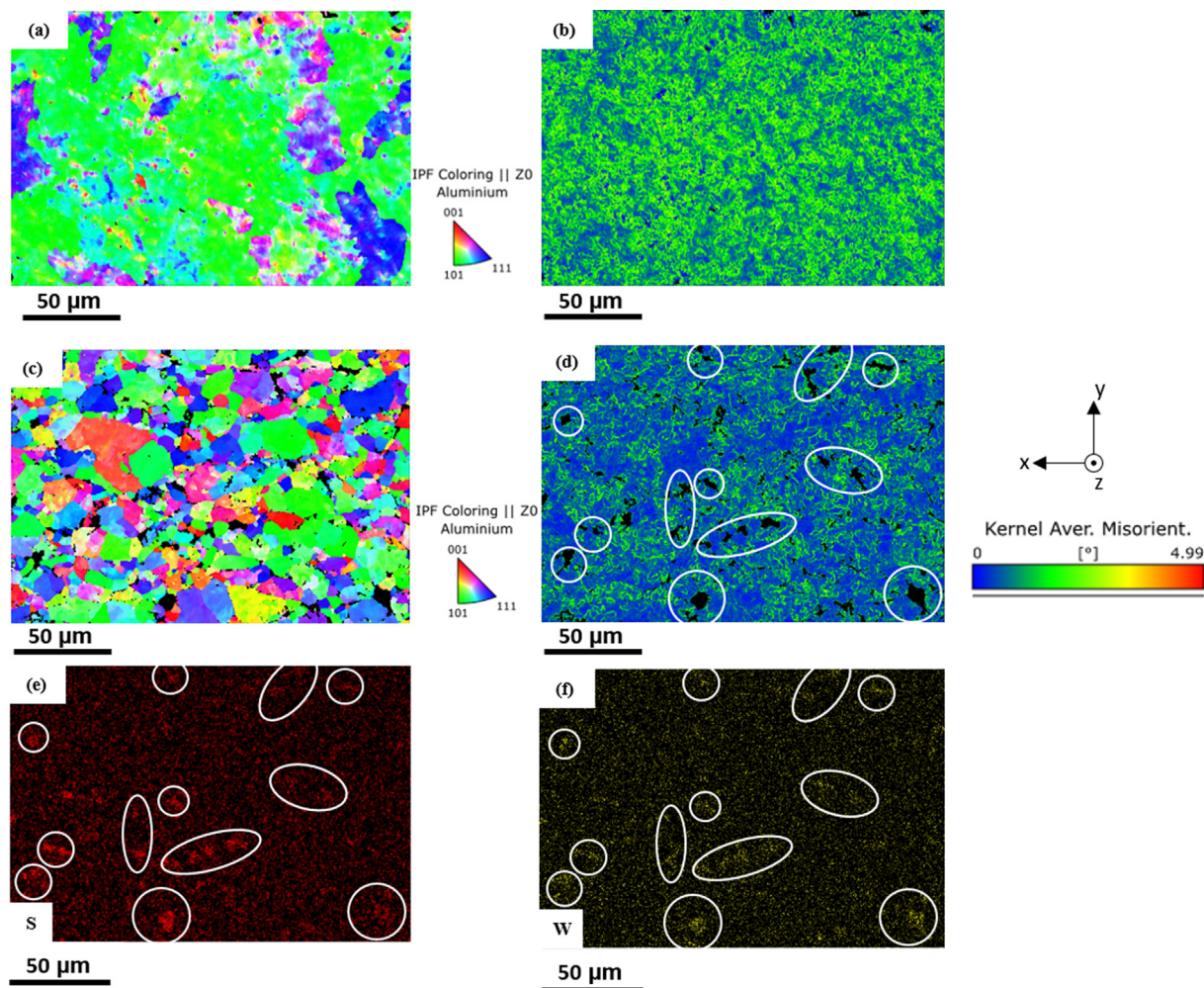
Fig. 9. High magnification IPF colour maps and KAM maps of the transverse cross-section (0.3 μm step size): (a) and (b) LPBF Al-WS$_2$; (c) and (d) SPS Al-WS$_2$; (e) and (f) the corresponding EDS maps of (c) and (d) for S and W, respectively.

Table 2
Microhardness and tribological results after 4000-cycle continuous wear for LPBF Al-WS$_2$, SPS Al-WS$_2$ and SPS Al.

Sample	Micro-hardness HV	Average COF (4000 cycles)	Specific wear rate$\times 10^{-3}$ mm^3/N·m
LPBF Al-WS$_2$	44.13 ± 7.2	0.55 ± 0.01	3.4 ± 0.3
SPS Al-WS$_2$	36.51 ± 1.23	0.57 ± 0.02	3.6 ± 0.3
SPS Al	34.35 ± 0.69	0.64 ± 0.02	5.4 ± 0.5

The WS$_2$ presented in the LPBF samples as nano-sized particles, and partial decomposition of WS$_2$ occurred, forming nanosized elementary S, W, micron-sized W particles, and the Al-W intermetallic phase in the matrix, while the WS$_2$-intermetallic-Al core–shell microstructure was yielded in SPS. The grains in LPBF parts exhibited a columnar morphology with relatively strong texture, in contrast to the SPS parts that showed no texture. The solid lubricant WS$_2$ and formed new phases with high hardness in the composite for both SPS and LPBF parts and were believed to result in enhanced tribological properties. LPBF Al-WS$_2$ exhibited the highest hardness as well as slightly reduced COF and wear rate compared to the SPS Al-WS$_2$. Nevertheless, this work also presented a new methodology for examining the evolution of the tribolayer at distinctive stages of wear. It was observed that the tribolayer formed earlier for the LPBF part. The wear-affected deforma-

tion depth in LPBF Al-WS$_2$ was also lower in comparison to SPS counterparts.

This is the first study to attempt and successfully report the in-situ production of Al-WS$_2$ composites using LPBF. These promising results proved LPBF as a viable technique for fabricating self-lubricating composites and pave the way for the utilisation of AM techniques in green tribological applications for enhanced performance and more sophisticated designs compared to the conventional manufacturing methods. From the tribological investigation of this study, it can also be asserted that not only will AM be advantageous from a design point of view in terms of manufacture, but also for the performance aspect. The intriguing finding that the in-situ reaction forms intermetallic phases with higher hardness at the expense of consuming the lubricating WS$_2$ as a trade-off opens up a new avenue of research in tailoring the processing parameters for in-situ microstructural control to maximise the tribological properties.

CRediT authorship contribution statement

Peifeng Li: Conceptualization, Methodology, Validation, Investigation, Writing – original draft, Data curation. **Fang Xu:** Supervision, Funding acquisition, Conceptualization, Resources, Writing – review & editing. **Stuart Robertson:** Investigation, Resources,
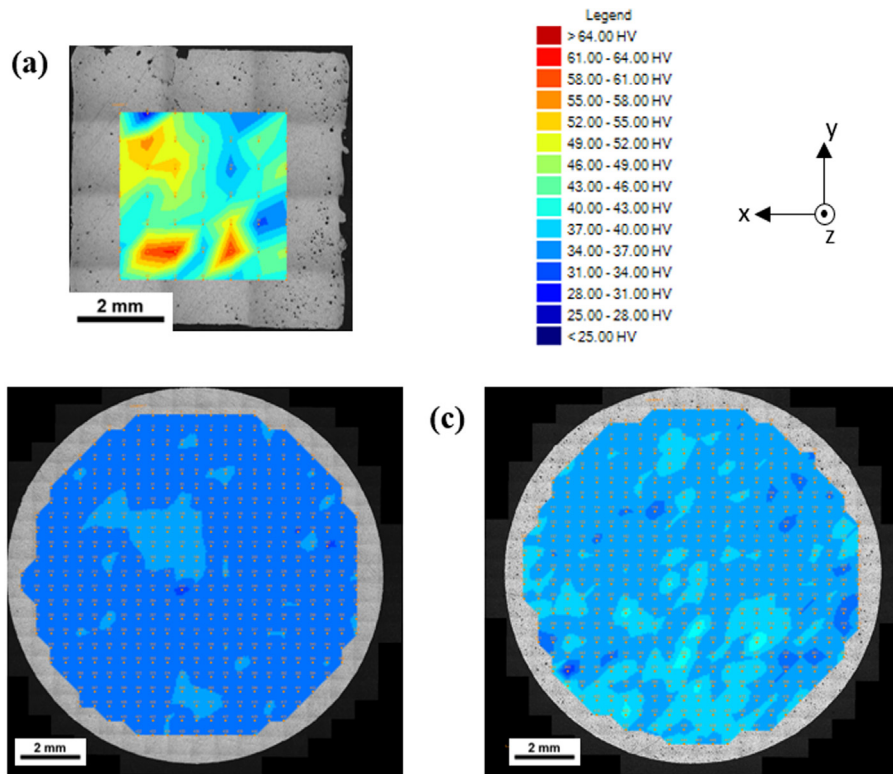
Fig. 10. Hardness data of the transverse cross-section. (a) LPBF Al-WS$_2$; (b) SPS Al; (c) SPS Al-WS$_2$. Colour print required.
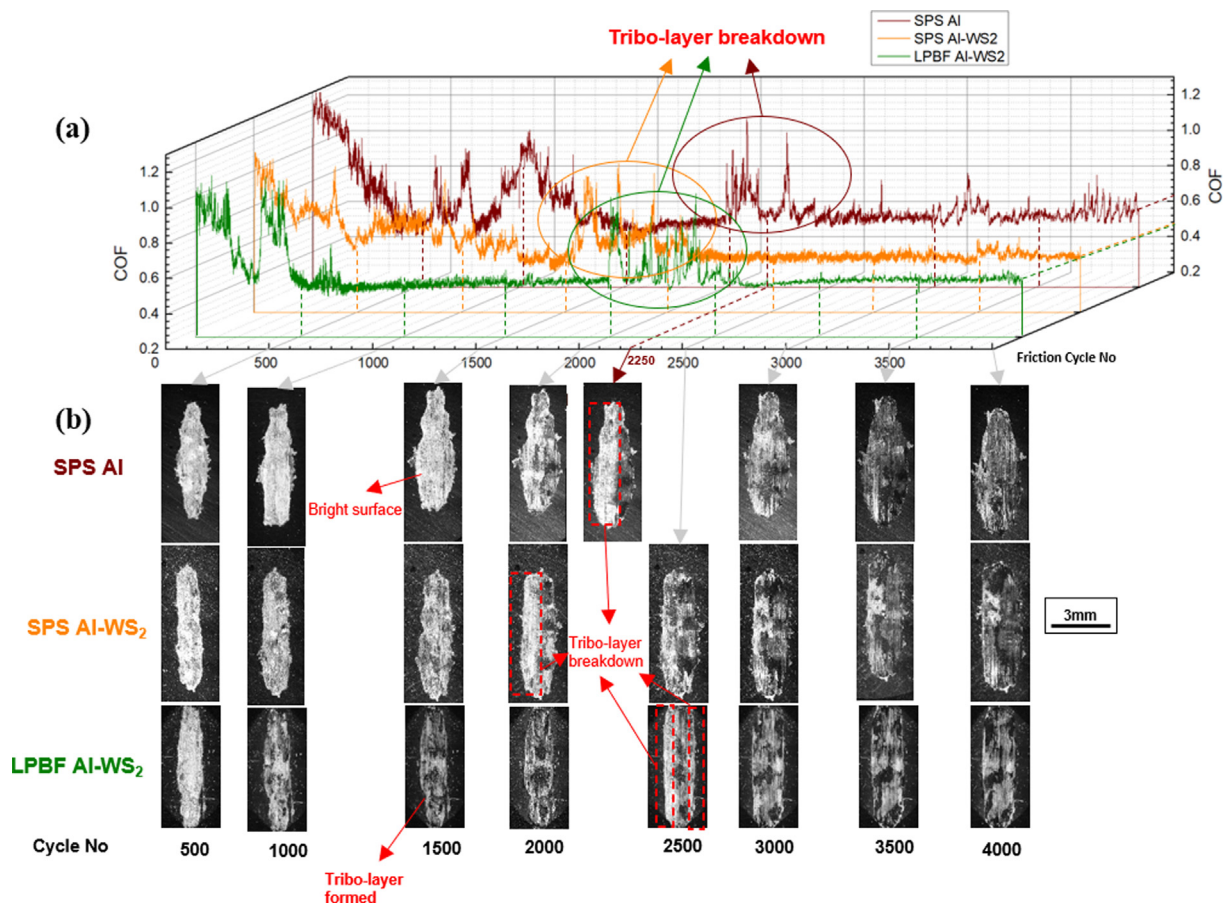

Fig. 11. Tribological results of the processed parts. (a) COF variation vs. Friction cycle curve for LPBF and SPS parts; (b) the evolution of wear track morphology during the 4000-cycle sliding wear test; Colour print required.

Table 3
Variation of specific wear rate at different sliding stages during 4000cycle wear test for SPS and LPBF parts.

Friction Cycles		0–1000	1000–2000	2000–3000	3000–4000
Wear Volume/$\times 10^{-3}$mm^3	LPBF Al-WS$_2$	364	–	76	–
	SPS Al-WS$_2$	396	144	72	–
	SPS Al	408	260	148	112
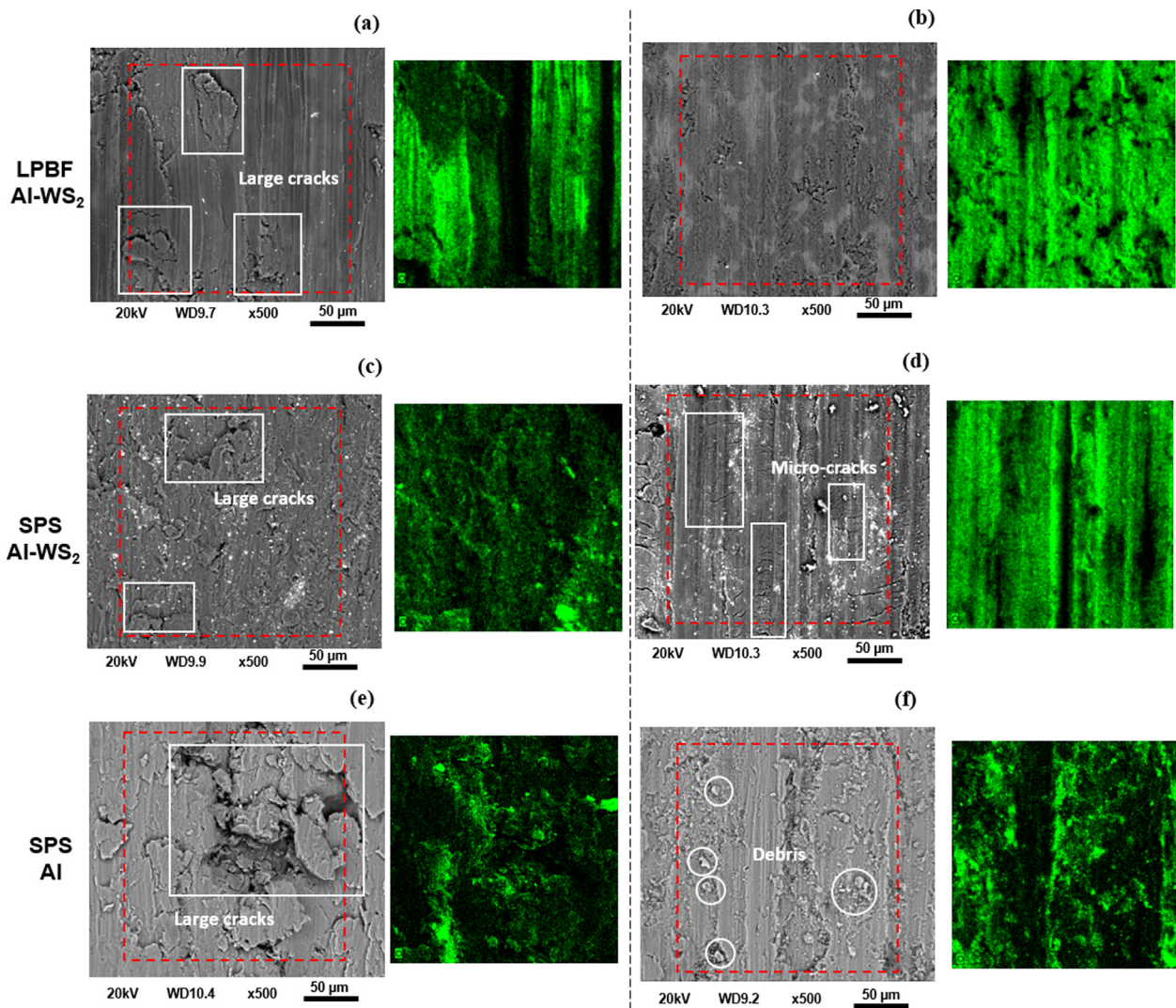
Fig. 12. SEM images of wear track morphology on various sample surfaces after different friction cycles and the O elemental distribution in the red frame area in SEM images. (a) LPBF Al-WS$_2$ after 500 cycles; (b) LPBF Al-WS$_2$ after 4000 cycles; (c) SPS Al-WS$_2$ after 500 cycles; (d) SPS Al-WS$_2$ after 4000 cycles; (e) SPS Al after 500 cycles; (f) SPS Al after 4000 cycles.

Table 4
The atomic ratio of elements on the worn surface of different samples obtained by EDX.

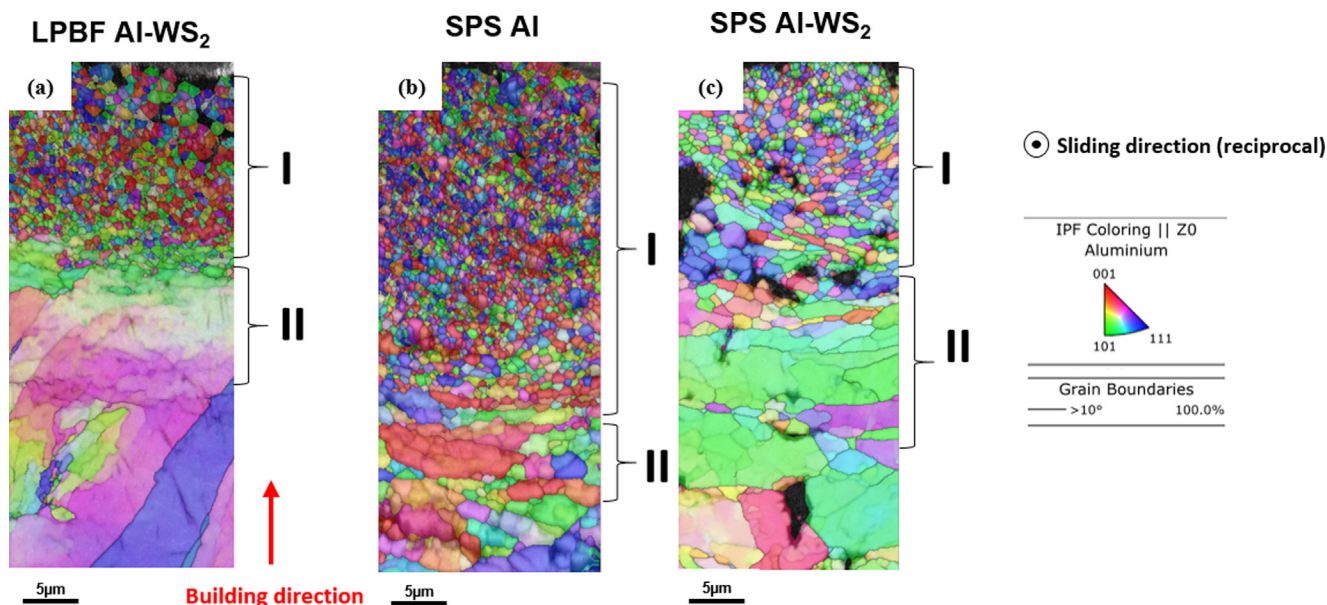| Atomic ratio/%	Al	O	W	S
LPBF Al-WS$_2$ 500 cycles	74.1	24.4	1.0	0.6
LPBF Al-WS$_2$ 4000 cycles	55.2	44.0	0.6	0.3
SPS Al-WS$_2$ 500 cycles	92.8	5.6	1.1	0.6
SPS Al-WS$_2$ 4000 cycles	67.3	31.8	0.6	0.3
SPS Al 500 cycles	95.0	5.0	–	–
SPS Al 4000 cycles	86.8	13.2	–	–

Fig. 13. Crystallographic depth profile of the vertical cross-section beneath the worn surface obtained via EBSD: (a) LPBF Al-WS$_2$; (b) SPS Al; (c) SPS Al-WS$_2$. Colour print required.

Writing – review & editing. **Zhaoxia Zhou:** Investigation, Resources, Writing – review & editing. **Xianghui Hou:** Supervision, Writing – review & editing. **Adam T. Clare:** Supervision, Writing – review & editing. **Nesma T. Aboulkhair:** Supervision, Funding acquisition, Resources, Conceptualization, Writing – review & editing.

Declaration of Competing Interest

The authors declare that they have no known competing financial interests or personal relationships that could have appeared to influence the work reported in this paper.

Acknowledgements

Data availability statement

The raw/processed data required to reproduce the findings of this study are available on request from the corresponding author [Fang Xu].

Appendix A. Supplementary material

Supplementary data to this article can be found online at https://doi.org/10.1016/j.matdes.2022.110543.

References

[1] S.V. Prasad, R. Asthana, Aluminum metal-matrix composites for automotive applications: tribological considerations, Tribol. Lett. 17 (3) (2004) 445–453, https://doi.org/10.1023/B:TRIL.0000044492.91991.f3.

[2] A.P. Hekimoğlu, M. Çaliş, Effects of titanium addition on structural, mechanical, tribological, and corrosion properties of Al–, Trans. Nonferr. Metals Soc. China 30 (2) (2020) 303–317, https://doi.org/10.1016/S1003-6326(20)65214-1.

[3] M.S. Khorrami, N. Saito, Y. Miyashita, M. Kondo, Texture variations and mechanical properties of aluminum during severe plastic deformation and friction stir processing with SiC nanoparticles, Mater. Sci. Eng., A 744 (2019) 349–364, https://doi.org/10.1016/j.msea.2018.12.031.

[4] N.S.M. El-Tayeb, K.O. Low, P.V. Brevern, Influence of roller burnishing contact width and burnishing orientation on surface quality and tribological behaviour of Aluminium 6061, J. Mater. Process. Technol. 186 (1-3) (2007) 272–278, https://doi.org/10.1016/j.jmatprotec.2006.12.044.

[5] M. Tabandeh-Khorshid, E. Omrani, P.L. Menezes, P.K. Rohatgi, Tribological performance of self-lubricating aluminum matrix nanocomposites: role of graphene nanoplatelets, Eng. Sci. Technol. Int. J. 19 (1) (2016) 463–469, https://doi.org/10.1016/j.jestch.2015.09.005.

[6] K. Edalati, M. Ashida, Z. Horita, T. Matsui, H. Kato, Wear resistance and tribological features of pure aluminum and Al–Al2O3 composites consolidated by high-pressure torsion, Wear 310 (1-2) (2014) 83–89, https://doi.org/10.1016/j.wear.2013.12.022.

[7] M.H. Rahman, H.M. Al Rashed, Characterization of silicon carbide reinforced aluminum matrix composites, Procedia Eng. 90 (2014) 103–109, https://doi.org/10.1016/j.proeng.2014.11.821.

[8] S. Mahdavi, F. Akhlaghi, Effect of the graphite content on the tribological behavior of Al/Gr and Al/30SiC/Gr composites processed by in situ powder metallurgy (IPM) method, Tribol. Lett. 44 (1) (2011) 1–12, https://doi.org/10.1007/s11249-011-9818-2.

[9] A. Sharma, A. Priyadarshini, R. Sujith, M.V.S. Subrahmanyam, P.A. Thomas, A.K. Gupta, Advanced Materials: Design, Processing, Characterization, and Applications 12 (2019), https://doi.org/10.1115/IMECE2019-10939.

[10] V.B. Niste, M. Ratoi, H. Tanaka, F. Xu, Y. Zhu, J. Sugimura, Self-lubricating Al-WS2 composites for efficient and greener tribological parts, Sci. Rep. 7 (2017) 1–14, https://doi.org/10.1038/s41598-017-15297-6.

[11] S. Rengifo, C. Zhang, S. Harimkar, B. Boesl, A. Agarwal, Effect of WS2 Addition on Tribological Behavior of Aluminum at Room and Elevated Temperatures, Tribol. Lett. 65 (2017) 76, https://doi.org/10.1007/s11249-017-0856-2.

[12] S. Alidokht, A. Abdollah-Zadeh, S. Soleymani, H. Assadi, Microstructure and tribological performance of an aluminium alloy based hybrid composite produced by friction stir processing, Mater. Des. 32 (2011) 2727–2733, https://doi.org/10.1016/j.pmatsci.2019.100578.

[13] K.S. Vinoth, R. Subramanian, S. Dharmalingam, B. Anandavel, Mechanical and tribological characteristics of stir-cast Al-Si10Mg and self-lubricating Al-Si10Mg/MoS2 composites, Mater. Technol. 46 (2012) 497–501.

[14] J. Xiao, Y. Wu, W. Zhang, J. Chen, C. Zhang, Friction of metal-matrix self-lubricating composites: Relationships among lubricant content, lubricating film coverage, and friction coefficient, Friction 8 (3) (2020) 517–530, https://doi.org/10.1007/s40544-019-0270-x.

[15] Z. Zhao, P. Bai, R.D.K. Misra, M. Dong, R. Guan, Y. Li, J. Zhang, L. Tan, J. Gao, T. Ding, W. Du, Z. Guo, AlSi10Mg alloy nanocomposites reinforced with aluminum-coated graphene: Selective laser melting, interfacial microstructure and property analysis, J. Alloy. Compd. 792 (2019) 203–214, https://doi.org/10.1016/j.jallcom.2019.04.007.

[16] S.F. Bartolucci, J. Paras, M.A. Rafiee, J. Rafiee, S. Lee, D. Kapoor, N. Koratkar, Graphene–aluminum nanocomposites, Mater. Sci. Eng., A 528 (27) (2011) 7933–7937, https://doi.org/10.1016/j.msea.2011.07.043.

[17] Y. Huang, M.C. Leu, J. Mazumder, A. Donmez, Additive manufacturing: current state, future potential, gaps and needs, and recommendations Article No. 014001, J. Manuf. Sci. En. 137 (2015), https://doi.org/10.1115/1.4028725.

[18] Q. Han, Y. Geng, R. Setchi, F. Lacan, D. Gu, S.L. Evans, Macro and nanoscale wear behaviour of Al-Al2O3 nanocomposites fabricated by selective laser melting, Compos. Part B: Eng. 127 (2017) 26–35, https://doi.org/10.1016/j.compositesb.2017.06.026.

[19] D. Gu, J. Jue, D. Dai, K. Lin, W. Chen, Effects of dry sliding conditions on wear properties of al-matrix composites produced by selective laser melting additive manufacturing, J. Tribol. 140 (2018) 021605, https://doi.org/10.1115/1.4037729.

[20] S.K. Ghosh, P. Saha, Crack and wear behavior of SiC particulate reinforced aluminium based metal matrix composite fabricated by direct metal laser sintering process, Mater. Des. 32 (1) (2011) 139–145, https://doi.org/10.1016/j.matdes.2010.06.020.

[21] L. Wu, Z. Zhao, P. Bai, W. Zhao, Y. Li, M. Liang, H. Liao, P. Huo, J. Li, Wear resistance of graphene nano-platelets (GNPs) reinforced AlSi10Mg matrix composite prepared by SLM, Appl. Surf. Sci. 503 (2020) 144156, https://doi.org/10.1016/j.apsusc.2019.144156.

[22] H. Salehi Vaziri, A. Shokuhfar, S.S. Seyyed Afghahi, Investigation of mechanical and tribological properties of aluminum reinforced with Tungsten Disulfide (WS2) nanoparticles, Mater. Res. Express 6 (4) (2019) 045018, https://doi.org/10.1088/2053-1591/aafa00.

[23] A.C. Domask, R.L. Gurunathan, S.E. Mohney, Transition Metal–MoS 2 Reactions: Review and Thermodynamic Predictions, J. Electron. Mater. 44 (11) (2015) 4065–4079, https://doi.org/10.1007/s11664-015-3956-5.

[24] A.C. Domask, K.A. Cooley, B. Kabius, M. Abraham, S.E. Mohney, Room temperature van der Waals epitaxy of metal thin films on molybdenum disulfide, Cryst. Growth Des. 18 (6) (2018) 3494–3501, https://doi.org/10.1021/acs.cgd.8b00257.

[25] F. Xu, T. Kobayashi, Z. Yang, T. Sekine, H. Chang, N. Wang, Y. Xia, Y. Zhu, How the toughest inorganic fullerene cages absorb shockwave pressures in a protective nanocomposite: experimental evidence from two in situ investigations, ACS Nano 11 (8) (2017) 8114–8121, https://doi.org/10.1021/acsnano.7b0294310.1021/acsnano.7b02943.s001.

[26] H. Tiismus, A. Kallaste, A. Belahcen, T. Vaimann, A. Rassõlkin, D. Lukichev, Hysteresis measurements and numerical losses segregation of additively manufactured silicon steel for 3D printing electrical machines, Appl. Sci. 10 (2020) 6515, https://doi.org/10.3390/app10186515.

[27] A. International, in: ASTM G133-05. (ASTM International, West Conshohocken, PA, 2016), vol. ASTM G133-05.

[28] N.T. Aboulkhair, M. Simonelli, L. Parry, I. Ashcroft, C. Tuck, R. Hague, 3D printing of Aluminium alloys: Additive Manufacturing of Aluminium alloys using selective laser melting, Prog. Mater Sci. 106 (2019) 100578, https://doi.org/10.1016/j.pmatsci.2019.100578.

[29] R. Li, Y. Shi, Z. Wang, Li. Wang, J. Liu, W. Jiang, Densification behavior of gas and water atomized 316L stainless steel powder during selective laser melting, Appl. Surf. Sci. 256 (13) (2010) 4350–4356, https://doi.org/10.1016/j.apsusc.2010.02.030.

[30] E. Louvis, P. Fox, C.J. Sutcliffe, Selective laser melting of aluminium components, J. Mater. Process. Technol. 211 (2) (2011) 275–284, https://doi.org/10.1016/j.jmatprotec.2010.09.019.

[31] K. Kempen, L. Thijs, J. Van Humbeeck, J.-P. Kruth, Processing AlSi10Mg by selective laser melting: parameter optimisation and material characterisation, Mater. Sci. Technol. 31 (8) (2015) 917–923, https://doi.org/10.1179/1743284714Y.0000000702.

[32] H. Kwon, D.H. Park, Y. Park, J.F. Silvain, A. Kawasaki, Y. Park, Spark plasma sintering behavior of pure aluminum depending on various sintering temperatures, Met. Mater. Int. 16 (1) (2010) 71–75, https://doi.org/10.1007/s12540-010-0071-2.

[33] D. Buchbinder, H. Schleifenbaum, S. Heidrich, W. Meiners, J. Bültmann, High power selective laser melting (HP SLM) of aluminum parts, Phys. Procedia 12 (2011) 271–278, https://doi.org/10.1016/j.phpro.2011.03.035.

[34] N.T. Aboulkhair, N.M. Everitt, I. Ashcroft, C. Tuck, Reducing porosity in AlSi10Mg parts processed by selective laser melting, Addit. Manuf. 1 (2014) 77–86, https://doi.org/10.1016/j.actamat.2015.06.004.

[35] C. Weingarten, D. Buchbinder, N. Pirch, W. Meiners, K. Wissenbach, R. Poprawe, Formation and reduction of hydrogen porosity during selective laser melting of AlSi10Mg, J. Mater. Process. Technol. 221 (2015) 112–120, https://doi.org/10.1016/j.jmatprotec.2015.02.013.

[36] A. Ramakrishnan, G.P. Dinda, Microstructural control of an Al–W aluminum matrix composite during direct laser metal deposition, J. Alloys Compd. 813 (2020) 152208, https://doi.org/10.1016/j.jallcom.2019.152208.

[37] A.G. Lekatou, M. Mpalanou, K. Lentzaris, A.E. Karantzalis, N. Melanitis, MATEC Web of Conferences, 188, EDP Sciences, 2018, p. 03001, https://doi.org/10.1051/matecconf/201818803001.

[38] A. Gencer, G. Surucu, Density functional theory (DFT) study of BaScO3H0. 5 compound and its hydrogen storage properties, Can. J. Phys. 97 (11) (2019) 1191–1199, https://doi.org/10.1139/cjp-2018-0733.

[39] M.J. Sayagués, J. Córdoba, F. Gotor, Room temperature mechanosynthesis of the La1− xSrxMnO3±δ (0≤ x≤ 1) system and microstructural study, J. Solid State Chem. 188 (2012) 11–16, https://doi.org/10.1016/j.jssc.2012.01.018.

[40] Q. Gao, H. Yan, Y. Qin, P. Zhang, J. Guo, Z. Chen, Z. Yu, Laser cladding Ti-Ni/TiN/TiW+ TiS/WS2 self-lubricating wear resistant composite coating on Ti-6Al-4V alloy, Opt. Laser Technol. 113 (2019) 182–191, https://doi.org/10.1016/j.optlastec.2018.12.046.

[41] A.H. Wang, X.L. Zhang, X.F. Zhang, X.Y. Qiao, H.G. Xu, C.S. Xie, Ni-based alloy/submicron WS2 self-lubricating composite coating synthesized by Nd:YAG laser cladding, Mater. Sci. Eng., A 475 (1-2) (2008) 312–318, https://doi.org/10.1016/j.msea.2007.04.087.

[42] H. Zhang, P. Feng, F. Akhtar, Aluminium matrix tungsten aluminide and tungsten reinforced composites by solid-state diffusion mechanism, Sci. Rep. 7 (2017) 1–8, https://doi.org/10.1038/s41598-017-12302-w.

[43] Q. Wang, M. Chen, Z. Shan, C. Sui, L. Zhang, S. Zhu, F. Wang, Comparative study of mechanical and wear behavior of Cu/WS2 composites fabricated by spark plasma sintering and hot pressing, J. Mater. Sci. Technol. 33 (11) (2017) 1416–1423, https://doi.org/10.1016/j.jmst.2017.06.014.

[44] E. Wiberg, N. Wiberg, A.F. Holleman, Inorganic Chemistry, 33th ed., Academic Press, San Diego, 2001.

[45] A.B. Kale, B.-K. Kim, D.-I. Kim, E.G. Castle, M. Reece, S.-H. Choi, An investigation of the corrosion behavior of 316L stainless steel fabricated by SLM and SPS techniques, Mater. Charact. 163 (2020) 110204, https://doi.org/10.1016/j.matchar.2020.110204.

[46] L. Thijs, K. Kempen, J.-P. Kruth, J. Van Humbeeck, Fine-structured aluminium products with controllable texture by selective laser melting of pre-alloyed AlSi10Mg powder, Acta Mater. 61 (5) (2013) 1809–1819, https://doi.org/10.1016/j.actamat.2012.11.052.

[47] K. Bertsch, G.M. de Bellefon, B. Kuehl, D. Thoma, Origin of dislocation structures in an additively manufactured austenitic stainless steel 316L, Acta Mater. 199 (2020) 19–33, https://doi.org/10.1016/j.actamat.2020.07.063.

[48] J.-K. Xiao, W. Zhang, C. Zhang, Microstructure evolution and tribological performance of Cu-WS2 self-lubricating composites, Wear 412 (2018) 109–119, https://doi.org/10.1016/j.wear.2018.07.024.

[49] R.L. Deuis, C. Subramanian, J.M. Yellup, Dry sliding wear of aluminium composites—a review, Compos. Sci. Technol. 57 (4) (1997) 415–435, https://doi.org/10.1016/S0266-3538(96)00167-4.

[50] H. Lee, K.I. Kim, J. Kim, M.-W. Pin, K.H. Oh, K.T. Kim, Electron microscopy characterization of the tribolayer formation mechanism in sintered Cu-based composites under dry sliding, Mater. Today Commun. 30 (2022) 103154, https://doi.org/10.1016/j.mtcomm.2022.103154.

[51] J.F. Archard, Contact and rubbing of flat surfaces, J. Appl. Phys. 24 (8) (1953) 981–988, https://doi.org/10.1063/1.1721448.

[52] Y. Liu, T.W. Liskiewicz, B.D. Beake, Dynamic changes of mechanical properties induced by friction in the Archard wear model, Wear 428–429 (2019) 366–375, https://doi.org/10.1016/j.wear.2019.04.004.

[53] D.K. Dwivedi, Adhesive wear behaviour of cast aluminium–silicon alloys: Overview, Mater. Des. (1980–2015) 31 (5) (2010) 2517–2531.

[54] T. Kayaba, K. Hokkirigawa, K. Kato, Analysis of the abrasive wear mechanism by successive observations of wear processes in a scanning electron microscope, Wear 110 (3-4) (1986) 419–430, https://doi.org/10.1016/0043-1648(86)90115-8.

[55] S.C. Gallo, H. Dong, EBSD and AFM observations of the microstructural changes induced by low temperature plasma carburising on AISI 316, Appl. Surf. Sci. 258 (1) (2011) 608–613, https://doi.org/10.1016/j.apsusc.2011.06.158.

[56] S. Nahata, M. Moradi, Y.N. Picard, N. Kota, O.B. Ozdoganlar, Micromachining imposed subsurface plastic deformation in single-crystal aluminum, Mater. Charact. 171 (2021) 110747, https://doi.org/10.1016/j.matchar.2020.110747.